To the Graduate Council:

I am submitting herewith a thesis written by Karen Thorbjornsen entitled "Three-Dimensional Development of a Natural Thrust-Related Fold: An Example From the Tuscarora Sandstone, Browns Mountain Anticlinorium, West Virginia." I have examined the final copy of this thesis for form and content and recommend that it be accepted in partial fulfillment of the requirements for the degree of Master of Science, with a major in Geology.

Dr. William M. Dunne, Major Professor

We have read this thesis and recommend its acceptance:

Prof. Robert D. Hatcher Jr.

Dr. Steven G. Driese

Accepted for the Council:

Associate Vice Chancellor and
Dean of The Graduate School

THREE-DIMENSIONAL DEVELOPMENT OF A NATURAL THRUST-RELATED FOLD: AN EXAMPLE FROM THE TUSCARORA SANDSTONE, BROWNS MOUNTAIN ANTICLINORIUM, WEST VIRGINIA

A Thesis
Presented for the
Master of Science
Degree
The University of Tennessee, Knoxville

Karen Thorbjornsen
December, 1995

DEDICATION

This thesis is dedicated to the memory of my father,

Dr. Arthur R. Thorbjornsen.

ACKNOWLEDGMENTS

This research was partially funded by grants from the American Association of Petroleum Geologists, the Geological Society of America, and Sigma Xi. I would like to thank Prof. Robert D. Hatcher Jr. and Dr. Steven G. Driese for their helpful comments in reviewing this manuscript in its various forms. I am also grateful to Prof. Hatcher for allowing me use of his MacIntosh computers. Dr. William M. Dunne deserves special thanks and a bouquet of rhododendron blossoms for accepting the role of my advisor and providing guidance and seemingly endless patience over the past few years.

I remain in Kevin Smart's debt for all of his assistance in the field and insights in the office, as well as for entrusting me with the return of his library books. To Tony Caldanaro, who came before, I extend my gratitude for his instruction in the use of the CL scope and thin-section polishing equipment, and for all other services rendered. Thanks, too, to Mark Carter for spending an afternoon assisting in the production of my geologic map, when I'm sure he had plenty of other things to do. The department secretaries -- Cindy Turner, Denise Stansberry, and Melody Branch -- and Prof. Hatcher's office manager Nancy Meadows were always helpful and courteous.

Certain individuals helped me in ways they never imagined. Dr. Stuart Dean, my undergraduate structural geology professor, introduced me to the geology of West Virginia and taught me that "zip, bang! - the structure solves itself." To Pam Spencer, I give my thanks for her understanding and moral support. I am grateful to Angie Harton for being a good listener and a captive audience for seminar and defense practice sessions. I lift a glass of Schwarze Katz to Paige Stafford for the long talks, cheap lunches, and good companionship; may she never forget her Viking roots. Donna Sharp provided amusement and psychological enlightenment, even during my darkest moments of digitizing.

I would not have achieved this degree without the wonderful role models I had for parents. To my mother, Leone Thorbjornsen, I offer loving thanks for her unwavering belief in me and her continual encouragement. Finally, my husband, Robert Fisher, has earned a special commendation for his patience, support, and inimitable sense of humor, which always lightened the load. I am grateful to him for always helping me put matters into perspective, no matter how clouded my judgment, and for putting up with me these past few years. *Quod erat faciendum.*

ABSTRACT

The purpose of this study is to test models for the origin of fault-related folds against a field example in order to determine which, if any, are viable. Although a variation of a model successfully fit the field example, a primary purpose of this work is not to propose a new model, but rather to show the need for multiple verifiable model tests in order to see which ones approximate reality. The Barclay anticline is a detached first-order parasitic fold to the Browns Mountain anticlinorium in the central Appalachians of West Virginia. It deforms the resistant Tuscarora Sandstone, which is exposed in two profiles, permitting comparison to models for fault-propagation folds, fault-bend folds, break thrusts, and folding that occurs after fault propagation. Geometry alone is an insufficient discriminator, because it eliminates only the fault-propagation fold model. Microscale deformation is also an insufficient discriminator, since it only records pervasive deformation resulting from diagenetic compaction and tectonic layer-parallel shortening, instead of the folding event. The distributions of layer-parallel slip surfaces, faults, and veins in the forelimb and hinge successfully differentiate between the fold models. The anticline exhibits preferential bedding-parallel slip in the forelimb with some hinge contraction, but no transport of material from forelimb to backlimb. Because folding occurred without material transport through the hinge, the anticline developed by break-thrusting with flexural slip and minor inner-arc contraction. Fold amplification occurred through hinge migration, perhaps because of kinking with only one rotating limb. Following thrust propagation, the anticline was translated through one footwall bend to its present position. The anticline did not develop self-similarly, which is consistent with a breakthrust origin.

TABLE OF CONTENTS

LIST OF TABLES

LIST OF FIGURES

FIGURE PAGE

LIST OF PLATES

PLATE PAGE

INTRODUCTION

Several different ideas have been proposed to explain the formation of an anticline with an imbricate thrust during deformation (Figure 1). For a fault-bend fold, the anticline is an artifact of the change in thrust trajectory (Rich 1934, Suppe 1983). With fault-propagation folds, the anticline amplifies in advance of, and as a product of, thrust propagation (Mitra 1990, Suppe & Medwedeff 1990, Fisher & Anastasio 1994). A break thrust forms when an anticline amplifies first and is offset later by the thrust (Willis 1893, Fischer *et al.* 1992, Morley 1994). Another model of fold-thrust development predicts the opposite in that the anticline amplifies after thrust propagation ceases, but while the thrust is still displacing (Armstrong & Bartley 1993). The treatise for each concept includes analyses of field examples that strongly support each case (Rich 1934, Mitra 1990, Fischer *et al.* 1992, Armstrong & Bartley 1993, Fisher & Anastasio 1994, Morley 1994). Hence, the interaction of anticlines and thrusts depends on the timing of thrust propagation and displacement with respect to fold amplification (Suppe & Medwedeff 1990, Fischer *et al.* 1992, Armstrong & Bartley 1993).

Closely tied to these ideas about thrust-related folding is the concept of self-similar growth, which occurs when the geometry of younger portions of a structure is identical to the earlier geometry in older parts of the structure (Suppe & Medwedeff 1990, Wilkerson *et al.* 1991, Fischer & Woodward 1992). A fold that exhibits self-similar growth, such as a fault-propagation fold, always has the same shape and position relative to the propagating thrust tip when viewed in sequential profiles along strike (Suppe & Medwedeff 1990, Fischer & Woodward 1992), and may be scale-dependent. This concept is in contrast to self-similar geometry, where geometric characteristics of a structure are scale-independent

Figure 1. Models for thrust-related folds. (a) Fault-bend fold (after Suppe 1983). (b) Fault-propagation fold (after Suppe & Medwedeff 1990). (c) Break-thrust fold (after Willis 1893). (d) Thrust-related fold of Armstrong & Bartley (1993).

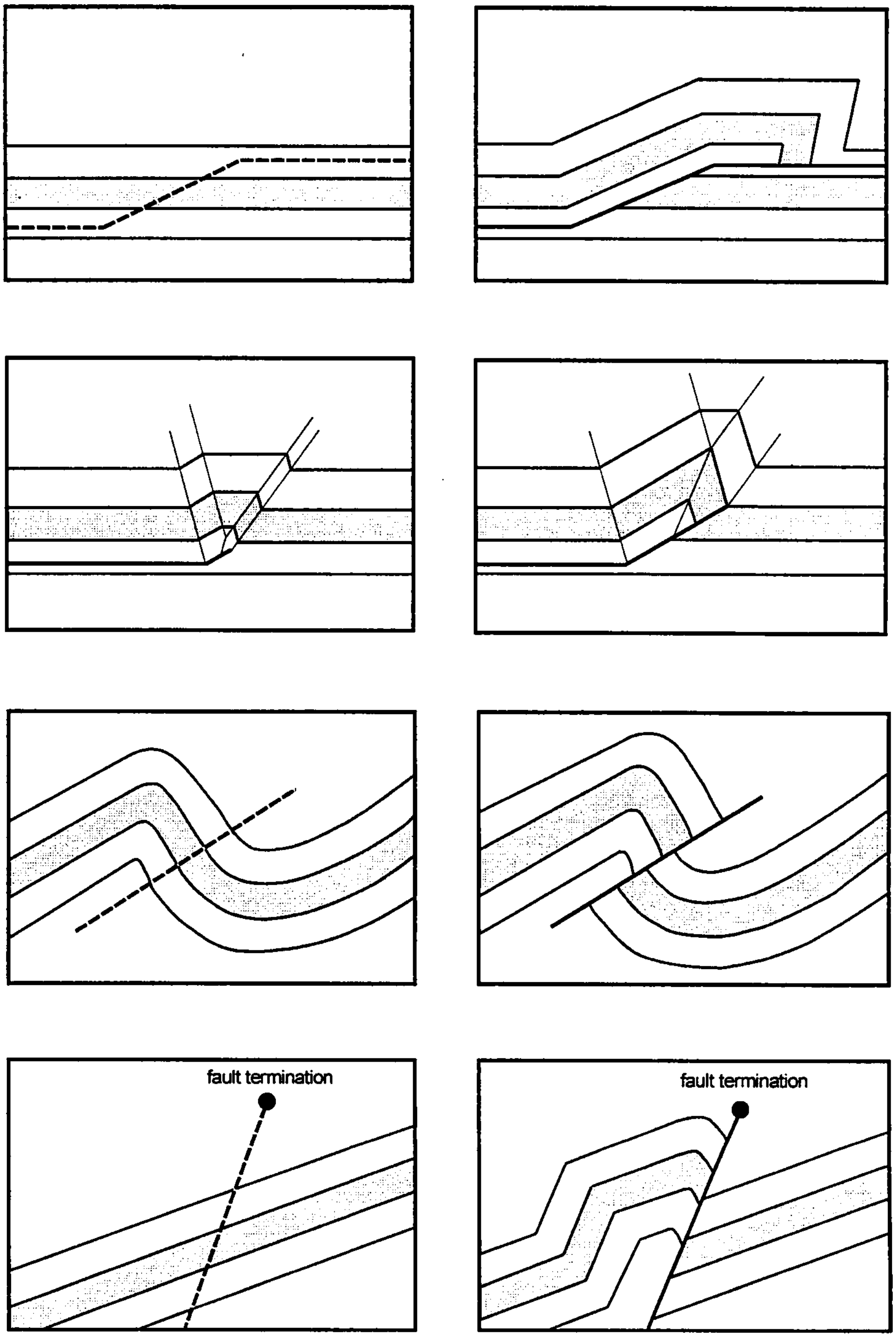

a.

b.

c.

d.

(Mandelbrot 1983, Wu 1993). This thesis only considers the first type of self-similarity.

Fault-bend and fault-propagation folds are commonly perceived to be self-similar (e.g., Wilkerson *et al.* 1991). Fault-bend folds form where thrusts step up in the direction of transport to a higher decollement and the thrust sheet rides over the bends in the fault (Faill 1973, Suppe 1983). According to Suppe, two kink bands form at the instant of initiation of slip. These bands increase in width and amplitude as the slip continues. When the kink bands stop growing, rock will continue to roll through the stationary axial surfaces with further displacement (Suppe 1983). Thus, fold geometry changes above a ramp through time at a given position and also changes above a thrust along fault strike as a function of thrust displacement.

With fault-propagation folds, anticlines grow up dip from the tips of propagating thrusts (Suppe & Medwedeff 1990). The amplitude of the anticlines accommodates profile shortening as displacement decreases to zero along the imbricate thrust. These folds exhibit self-similar growth by kink-band migration. The fold always has the same shape and position relative to the propagating fault tip but grows in size by beds rolling through the kink-band boundaries as the fault propagates. A fault-propagation fold will cease to grow self-similarly when the imbricate thrust breaks through the structure, usually along a decollement, within the steep limb or the anticlinal core (Suppe & Medwedeff 1990). A field study supports the applicability of self-similar growth to fault-propagation folding (Fisher & Anastasio 1994), demonstrating that geometry, finite strain, and incremental strain paths are self-similar between two profiles of the same structure.

Whereas fault-propagation and fault-bend folds may form self-similarly, the two other classes of fault-related folds in which folding and faulting are diachronous may not. Field study of break thrusts indicates that the fold geometry at a thrust termination could not evolve into the fold geometry at the site of greatest thrust displacement. Fold development results from variation in stratigraphy and resulting variation in structural competency (Fischer & Woodward 1992). Consequently, cutoff angles vary between successive cross sections along the structural trend, and the mode of thrust propagation varies, as well. Self-similarity dictates uniformity of geometric characteristics (Suppe & Medwedeff 1990, Fischer & Woodward 1992). Features such as fold shape, interlimb angle, and cutoff angle are preserved during growth of the structure. When these characteristics are not preserved, as with break-thrusting, then fold formation is not self-similar (Fischer & Woodward 1992).

For the case in which folding occurs mostly after fault propagation (Armstrong & Bartley 1993), the geometry of the folds at the thrust termination could not evolve into the geometry at the site of greatest thrust displacement. Fault propagation ceases when the lateral tip of the thrust locks, probably due to along-strike thickness changes in the competent unit. Also, Armstrong and Bartley (1992) noted that the kinematic behavior changes northwest of the lateral tip from thrust-related simple shear to transpression. These interpretations are incompatible with self-similarity. Another problem for a self-similar interpretation is that twinned calcite strain data indicate homogeneous strain throughout the structure. If the anticline were a break thrust or a fault-propagation structure, strain should vary as a function of position in the fold. Armstrong & Bartley (1993) interpret the homogeneous distribution of strain to indicate that the fold intstead formed by a different mechanism: folding to absorb displacement after fault propagation.

The objectives of this thesis are: (1) to use the exposed geometry of a thrust-related anticline to determine the interaction between fold growth and thrust propagation; (2) to test the applicability of current kinematic ideas for thrust-related folds to the structure; and (3) to determine if the structure developed in a self-similar manner. Data were collected at a variety of scales for these objectives. A large-scale (1:2400) geologic map and two cross sections were constructed to define the geometry of the fold-thrust system. Microstructures and mesostructures were identified and their orientations and relative abundances measured to provide information on deformation intensity, geometry, and the possible location of pin lines. Finally, finite and incremental strains were calculated from the normalized Fry and pressure solution methods (Erslev 1988, Onasch 1993) to provide kinematic data for this study.

GEOLOGIC SETTING

Regional geology

The study area is in southeastern West Virginia in the Plateau of the central Appalachians (Figure 2). The thrust-related fold under scrutiny, the Barclay anticline, is located in the Browns Mountain anticlinorium. This anticlinorium formed in the roof sequence above a blind duplex containing Cambro-Ordovician carbonates (Kulander 1968, Cecil 1972, Kulander *et al.* 1986). The anticlinorium is an unusual structure in the Appalachian Plateau because blind duplexes are rare in the Cambro-Ordovician carbonates of this region. The Tuscarora Sandstone was buried about 4.5 km by a Silurian to possibly Permian sequence (Colton 1970, Chen 1981), at temperatures of 150-200° C from color-alteration indices of conodonts in overlying Silurian limestones (Harris 1979).

The anticlinorium contains a total of three first-order parasitic structures, but they change type eastward with position: an anticline, a thrust-anticline combination, and a thrust fault. Exposures of the thrust-anticline combination, the Barclay anticline and thrust, are the target for this investigation (Figure 2). These structures contain many smaller second-order parasitic folds in sandstone units. Additional smaller folds are best developed in ductile shales and thin-bedded siltstone and limestone units (Cecil 1972, Kulander *et al.* 1986).

Target stratigraphic unit

The target stratigraphic unit is the Tuscarora Sandstone of Lower Silurian (Figures 2, A.1), which consists of planar to cross-bedded, locally

Figure 2. Stratigraphic column and geologic map of study area in Pocahontas County, West Virginia. A-A' and B-B' are section lines in Figure 3.

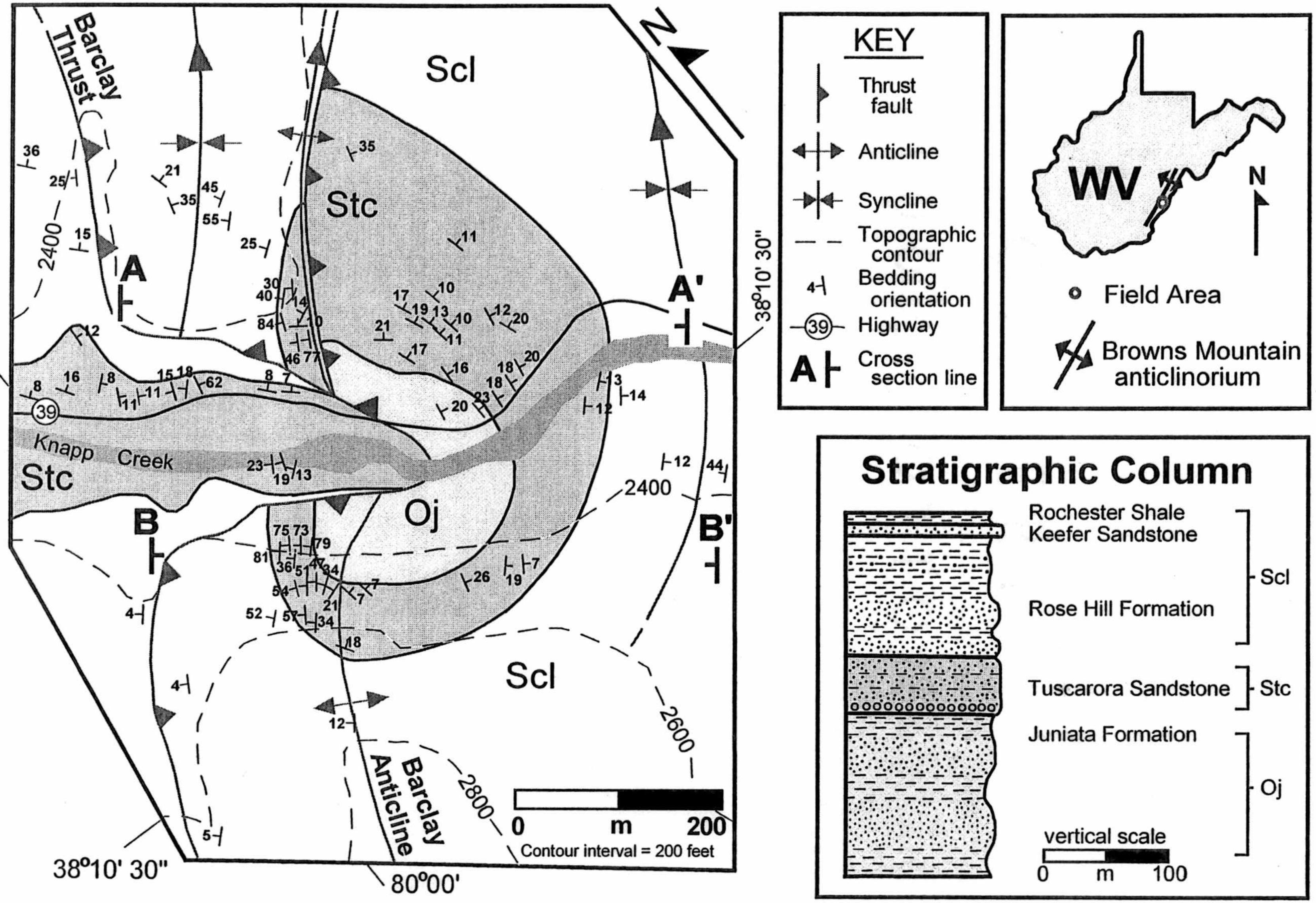

Barclay Thrust
Scl
Stc
Oj
Knapp Creek
39
A
A'
B
B'
2400
2600
2800
80°00'
38°10' 30"
Barclay Anticline
N
0 m 200
Contour interval = 200 feet
KEY
Thrust fault
Anticline
Syncline
Topographic contour
Bedding orientation
Highway
Cross section line
WV
N
Field Area
Browns Mountain anticlinorium
Stratigraphic Column
Rochester Shale
Keefer Sandstone
Rose Hill Formation
Scl
Tuscarora Sandstone
Stc
Juniata Formation
Oj
vertical scale
0 m 100

burrowed, well-sorted quartz arenite (Cecil 1972, Kulander *et al.* 1986) and has a thickness of 47 m in the study area. The Tuscarora Sandstone is characterized by a massive pebble conglomerate at the contact with the Juniata Formation (Bambach 1987, Dorsch *et al.* 1994), and can be subdivided into a lower massive unit and an upper massive unit (Figure A.1). The lower unit consists of light gray, thin- to medium-bedded quartz arenite with thin siltstone interbeds. The upper unit consists of medium to thick-bedded, clean, white, coarse- to medium-grained quartz arenite (Bambach 1987, Dorsch *et al.* 1994). This unit is essentially monomineralic and is highly resistant to weathering, yielding outcrops in most structural domains. The framework-supported texture of quartz arenites (Hayes 1974) is well suited for strain analysis using spatial techniques, such as the normalized Fry method (Erslev 1988).

In the study area, the resistant sandstone units of the Tuscarora Sandstone are exposed as three geomorphological "ribs" in the hanging wall. These exposures run across strike, revealing the forelimb, hinge, and adjacent backlimb, but are only meters to tens of meters thick vertically. The lowermost exposure is the thickest at 25 m, and is locally divisible into two sections in some places. The upper Tuscarora Sandstone is characterized by two geomorphological "racetracks" of shale and siltstone sandwiched between the quartz arenite layers. Although these lithologically distinct units are covered in the study area, they average about 4.5 m in thickness in nearby exposures. Because of these weak units the Tuscarora Sandstone contains three mechanically important sandstone layers.

In addition to the Tuscarora Sandstone, the study area includes four other stratigraphic units (Cecil 1972, Kulander *et al.* 1986)(Figure 2). Underlying the Tuscarora Sandstone is the Upper Ordovician (Ashgillian) Juniata Formation, which consists of terrigenous red sandstone and shale. Immediately overlying the Tuscarora Sandstone in the field area is the Middle Silurian Rose Hill Formation (Clinton Group). The lower part of the Rose Hill Formation contains mostly hematite-cemented quartz sandstone. The upper part of the Rose Hill Formation consists of olive-green to brown shale and thin siltstone units (Cecil 1972). Overlying the Rose Hill Formation is the Keefer Sandstone, a gray to white, fine-grained, hematitic sandstone. The gray, fissile Rochester Shale is the uppermost unit of the Clinton Group.

MAP-SCALE STRUCTURAL GEOMETRY

The Barclay anticline, so named due to its proximity to the gully Barclay Run, is well exposed in the two slopes on either side of Highway 39 and Knapp Creek, between the villages of Minnehaha Springs and Huntersville. Two cross sections were constructed to represent the geometry of the two exposures of the anticline (Figure 3). The constraints for cross-section construction are: (1) the surface geology includes abundant exposures of Tuscarora Sandstone that provide bedding orientation data and locations of some stratigraphic contacts, and which clearly define fold geometry (Appendix A); (2) the stratigraphic thickness of 47 m for the Tuscarora Sandstone was measured from an undeformed section within one kilometer east of the field area; (3) the crest of the anticline in the Tuscarora Sandstone of the hanging wall of the Barclay thrust is topographically higher to the southwest, whereas the top of the Tuscarora Sandstone in the footwall of both profiles is at about the same elevation; (4) stratigraphic omission of hanging wall rocks of the northern profile indicates the presence of an additional thrust fault in that profile.

Several assumptions were made in constructing the cross sections: (1) bedding thickness is preserved and a parallel fold geometry is assumed, which is consistent with field observations; (2) the thrusts were assumed to predate smaller folds in the footwall, and hence is folded by them; (3) the thickness of the Juniata Formation in the hanging wall between the Tuscarora Sandstone of the footwall and hanging wall is used to define the depth to the floor thrust, and this depth increases to the southwest; (4) the dip of the thrust is assumed to mimic the dip of bedding in the hanging wall, except beneath

Figure 3. (a) Cross section along line A-A' (Figure 2). (b) Cross section along line B-B' (Figure 2). Tick marks denote location of bedding orientation measurements.

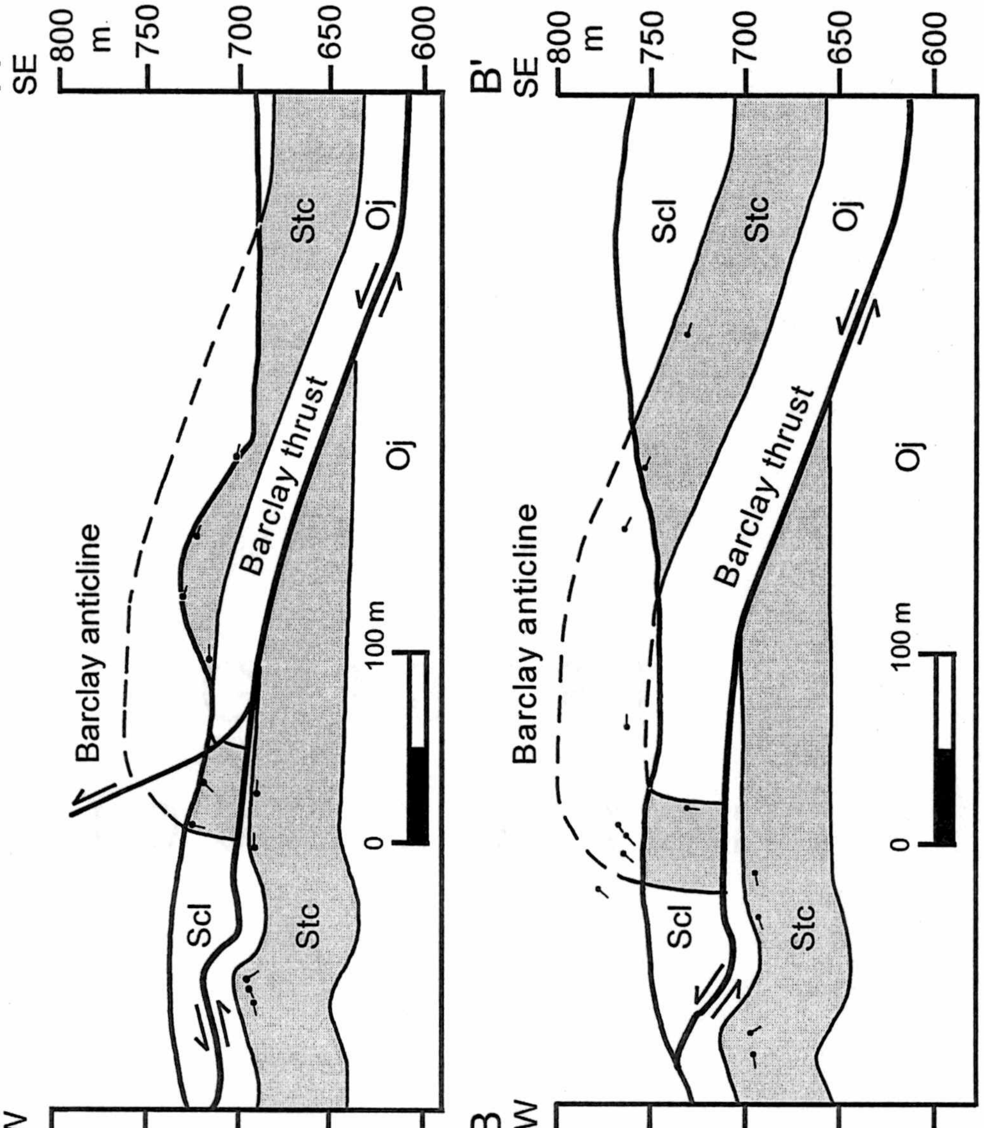
a.
A
NW
800
m
750
700
650
600
Scl
Stc
Barclay anticline
Barclay thrust
Oj
0
100 m
Stc
Oj
A'
SE
800
m
750
700
650
600
b.
B
NW
800
m
750
700
650
600
Scl
Stc
Barclay anticline
Barclay thrust
Oj
0
100 m
Scl
Stc
Oj
B'
SE
800
m
750
700
650
600

the hanging wall ramp; (5) because the last-exposed footwall rocks closest to the footwall ramp contain flat-lying rocks, the unexposed portion of the footwall ramp is inferred to be flat.

The anticline has a subvertical forelimb in both cross sections, along with a narrow rounded hinge, and a backlimb that steepens from flat over the roof thrust to a 20° SE dip parallel to the footwall ramp. The thrust consists of a roof flat at a small angle to bedding, a footwall ramp with a stratigraphic relief of about 85 m, and a floor thrust parallel to bedding. The thrust and anticline geometry change over the 244 m between the two profiles (Table 1). In the direction of plungeout to the northeast, displacement decreases along the fault by 36 m, the footwall ramp angle shallows by 3.5°, fold wavelength shortens by 46 m, fold amplitude decreases by 31 m, and an imbricate thrust appears in the backlimb. In addition, the depth to detachment in the Juniata Formation decreases by 18 m, indicating that the thrust here lies along an oblique ramp.

The imbricate thrust in the hinge zone of the northern profile is interpreted to have formed during folding. Had the fault formed prior to development of the Barclay anticline and thrust (Figure 4a), much less Juniata Formation would be present in the imbricate footwall than is indicated by field stratigraphic relationships (Figure 3). If the fault postdated the Barclay thrust, it would have displaced the Barclay thrust and its footwall rocks (Figure 4b). Such displacement is not evident in the field area. Hence, the imbricate fault is most likely a synfaulting structure.

An alternative interpretation of the overall map-scale geometry is possible. The presence of smaller folds in the footwall to the northwest of the Barclay anticline and thrust could reasonably indicate by analogy that such folds

Table 1. Fold geometry data.

Parameter	North Profile A-A'	South Profile B-B'
Displacement (m)	110	146
Ramp angle (deg.)	20	22
Wavelength (m)	113	159
Amplitude (m)	70	101
Interlimb angle (deg.)	97	94

Figure 4. Alternative explanations for development of imbricate thrust in northern fold profile. (a) Fault formation prior to development of Barclay anticline and thrust. (b) Fault formation postdating development of Barclay anticline and thrust.

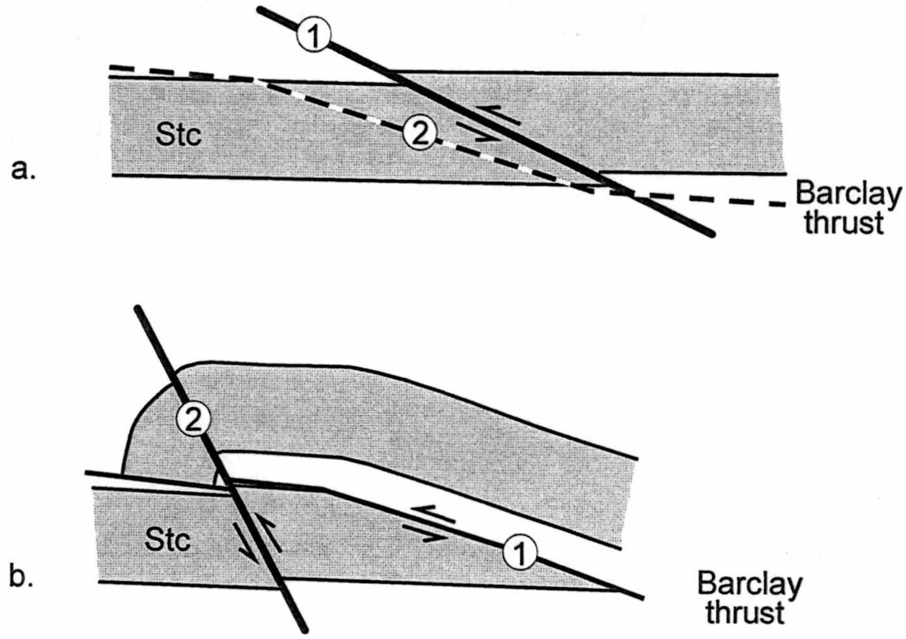
a.
1
Stc
2
Barclay
thrust
b.
2
Stc
1
Barclay
thrust

would be present in the footwall in the area where lack of exposure precludes data collection. These smaller folds, if present, would therefore deform the thrust surface and contacts in the hanging wall. The author prefers the first interpretation based on data from the continuously exposed Tuscarora Sandstone in the southeastern limb of the Barclay anticline adjacent to the northern profile (A-A'). When dip data from these rocks are projected into A-A', the apparent dips range from 0° to 15° SE with a systematic increase in dip magnitude from northwest to southeast. Nowhere in the exposed southeast limb do rocks dip to the northwest. The lack of northwest dips and the systematic increase in dips to the southeast are not consistent with the shapes of the small folds in the footwall to the northwest, although small folds could die out upward into the Juniata Formation. Thus, this interpretation was not applied to the study area.

Another suggested interpretation is that northwest-southeast trending cross-folds exist in the middle of the study area. Such cross-folds require rocks to be dipping either northeast or southwest. The field area contains several locations in the footwall and hinge of the Barclay anticline where rocks dip to the northeast. Nowhere in the study area, however, are rocks exposed that dip to the southwest. Additionally, these northeast dips are consistent with the regional northeast plunge of the Barclay anticline and the northeast plunge of the host Browns Mountain anticlinorium (Cardwell *et al.* 1968, Kulander 1968, Kulander *et al.* 1986). Therefore, the author does not believe that sufficient data exist to support an interpretation of cross-folding. The occurrences of the northeast dip of bedding may be more simply explained as being a result of axial plunge of both the Barclay and Browns Mountain anticlines.

Model predictions vs. fold geometry

The present position of the Barclay anticline involved passage through one or more fault bends (Figures 1 and 3), but this fault-bend folding need not be the initial cause for growth of the anticline. The anticline could have formed as any of the kinematic types and then have been translated through the fault bend(s) (Mitra 1990, Suppe & Medwedeff 1990, Fischer *et al* 1992). Possible deformation patterns from four models of fold-thrust development were calculated for the fold geometry in profile B-B' (Figure 5). These predicted patterns will be compared to microstructural distributions, mesostructural distributions, and measured strains in the fold to test the applicability of each model to fold development.

Combinations of five end-member deformations were calculated for each model (Table 2, Figure 4). For these equations, S is layer-parallel slip, t is mechanical layer thickness, θ is the dip of the layer in radians, and θ_o is the maximum ramp dip. Gamma is the shear strain, R is the aspect ratio of the finite strain ellipse, and θ'' is the angle between the long axis of the finite strain ellipse and bedding. The parameter L_1 is the length of neutral surface in fold profile, and L_2 is the length of the outer arc in fold profile. For $\beta = \pi / S_o$, the variable S_o is equal to one-half of the arc length of the fault-bend fold at the top of the bending layer.

Many variations for fault-propagation folding exist (e.g., Mitra 1990, Suppe & Medwedeff 1990, Morley 1994, McConnell 1994), but the only applicable one that is consistent with the outcrops of the Tuscarora Sandstone has constant bed thickness. This model fails to yield the geometry of the natural fold (Figure 5a). It requires an overturned forelimb dipping 76° SE and an

Figure 5. Predicted deformation patterns: (a) fault-propagation fold (Suppe & Medwedeff 1990), (b) fault-bend fold (Suppe 1983), (c) folding-after-fault propagation (Armstrong & Bartley 1993), and (d) break-thrust fold (Fischer *et al.* 1992). Deformation patterns are superimposed on the fold shape of profile B-B' (Figure 3). Light gray ellipses represent bending strains, black ellipses represent flexural flow, and numbers with shear arrows represent the magnitude of layer-parallel slip across the 47.2-m thickness of Tuscarora Sandstone. The break-thrust fold (d) is the only model that could contain a pinline in the hinge.

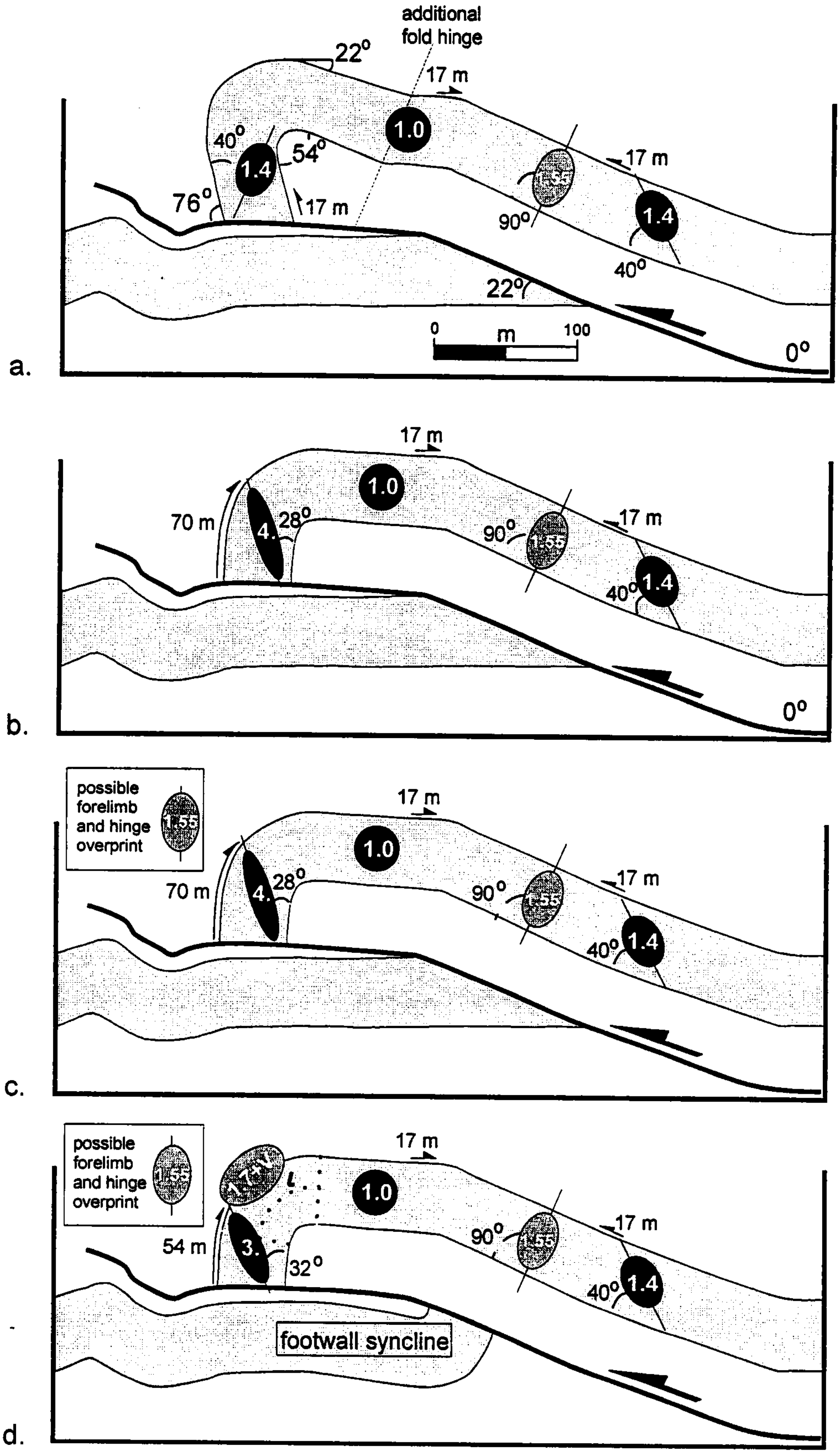
additional fold hinge
22°
17 m
1.0
40°
1.4
54°
76°
17 m
1.55
17 m
90°
1.4
40°
22°
0 m 100
0°
a.
17 m
1.0
70 m
4.
28°
90°
1.55
17 m
40°
1.4
0°
b.
possible forelimb and hinge overprint
1.55
17 m
1.0
70 m
4.
28°
90°
1.55
17 m
40°
1.4
c.
possible forelimb and hinge overprint
1.55
17 m
1.0
54 m
3.
32°
90°
1.55
17 m
40°
1.4
footwall syncline
d.

Table 2. Equations for end-member deformations (Figure 4).

Deformation	Equation	Source
layer-parallel slip	$S = t\theta$	eq. #7-38, Ramsay (1967)
simple shear	$\gamma = \theta$	p. 3, Ramsay & Huber (1983)
flexural flow	$R = \dfrac{2+\gamma^2+\gamma(\gamma^2+4)^{1/2}}{2}$ $\theta'' = \dfrac{\gamma+(\tan^{-1}(2/\gamma))}{2}$	eq. #21.7 & 21.8, Ramsay & Huber (1987)
bending strain (above fault bends)	$\varepsilon = \dfrac{t\theta_o\beta}{4}$	eq. #3c, Wiltschko *et al.* (1985)
bending strain (in other fold hinges)	$\dfrac{L_2}{L_1} \times 100$	

interlimb angle of 54°. Neither of the natural fold profiles exhibits this geometry, because both have forelimbs that dip 75-85° NW and have interlimb angles of 94-99°. Additionally, the fault-propagation fold model requires the presence of a second fold hinge and an axial surface above the roof flat (Figure 5a) to accommodate the combination of fault-bend and fault-propagation folding. Neither natural fold profiles contains such a feature. Figure 5(a) illustrates possible internal deformations for fault-propagation folding, but they will not be described because the model fails geometrically.

The other three models successfully yield the interpreted geometry of the Barclay anticline, showing that fold geometry is an insufficient discriminator between them. Hence, they need to be compared kinematically for differences. All three models satisfy the exposed fold geometry in the backlimb similarly. The change in backlimb dip is interpreted to be the result of a footwall ramp (Figure 3). The steeper portion of the backlimb is above the ramp and this part of the hanging wall has only passed through one fault bend. Thus, for all four models, the deformation derives from emplacement of the backlimb on the ramp (Figure 5). If deformation was through layer-parallel slip, the 47 m of the Tuscarora Sandstone with a ramp angle of 22° (Table 1) requires 16.5 m of slip between top and bottom. Layer-parallel simple shear instead produces a distortion with an ellipse of R = 1.42 and θ" = 40°. Alternately, if emplacement was achieved by bending, the layer would shorten up to 20% in the inner arc, producing a strain with an ellipse ratio R of 1.56 and θ" of 90°. This bending strain was calculated for a mechanical strut with a 25-m maximum thickness. The Tuscarora Sandstone would not act as a single bending member of 47 m because it includes an 11-m sequence of quartz-rich siltstone and shale about 25 m above its base. In the study area and at other excellent exposures of Tuscarora Sandstone within a 2.5 km radius of the area, these less competent sequences allow different intervals of the strong unit to slip independently.

The frontal part of the backlimb, where bedding dip is nearly horizontal, is interpreted as being above a roof flat (Figure 3). Here, the sandstone in the hanging wall passed through two fault bends. Consequently, the rocks would have folded and then unfolded (Sanderson 1982). Such reciprocal deformation should be expected to yield near-zero finite strains with strain ratios of 1.0 (Figure 5). Although the rocks would appear to have no finite strain, structural suites could reflect this sequential reciprocal deformation. Contractional micro- and mesostructures would form during passage through the lower fault bend and would be overprinted by extensional features formed as a result of passage through the upper fault bend. The presence of such suites will be discussed in subsequent sections on small-scale structures.

The magnitudes of end-member behavior calculated for the backlimb reflect the maximum values possible for each component of deformation. These kinematic behaviors may have occurred concurrently, necessitating smaller values for each component. The structural suites and measured strains to be described in the next four sections of this thesis will be used to interpret whether deformation consisted of one or more behaviors. The following description of deformation magnitudes for other portions of the folds also utilize end members to highlight differences in behavior.

The models predict deformation differences in the hinge and forelimb. If fault-bend folding occurred, the hangingwall cutoff angle changed during displacement from 22° to 85° (Figures 5b and 6). For a forelimb dip of 85° and a unit thickness of 47 m, this change could be achieved through 70 m of layer-parallel slip, or through flexural flow with shear strain of 1.5 for a strain ratio of 4.0 and θ" of 28°. These deformations cause a relative displacement of the top of the Tuscarora Sandstone through the main fold hinge with respect to base (Figure 6). Thus, folding in this model could not be pinned in the main hinge. For the third case, in which folding follows fault propagation, deformation would initially resemble that of fault-bend folding, because the fold developed after passage of the fault tip, and the cutoff angle is modified during folding (Figures 5b and 5c). The similarity of fold shape and formation after fault propagation implies that deformation magnitudes should be the same as those for fault-bend folding, and the main hinge would also lack a pinline. The fold forms prior to passage through the upper fault bend of the footwall ramp, so the fold should record an additional deformation during passage through the bend. Overprinting in a folded sedimentary sequence could be complex and lithologically dependent. In a simple case, it could be bending with up to 20% extension, which produces a strain ratio R of 1.6 and θ" of 90°.

If break-thrust folding occurred, the footwall should contain a syncline (Figure 5d). Although much of the footwall is exposed and is flat-lying, the 20 m closest to the footwall ramp is unexposed. Cross sections were constructed using the simplest geometry, which includes an unfolded footwall, although a footwall syncline cannot be excluded as a possible geometry.

If the hanging-wall cutoff angle was preserved during displacement of the forelimb by break-thrusting (Fischer *et al.* 1992), the initial forelimb dip was 63° NW. For this dip, if the forelimb sheared during initial buckle folding, forelimb deformation could consist of 54 m of layer-parallel slip, or perhaps simple shear

Figure 6. Change in hanging-wall cutoff angle during passage of rock from the footwall ramp onto the roof thrust in a fault-bend fold. (a) Position of Tuscarora Sandstone before thrusting. (b) Position of Tuscarora Sandstone after thrusting. Shaded area represents the volume of rock that must displace backwards to accommodate the change in cutoff angle.

a.

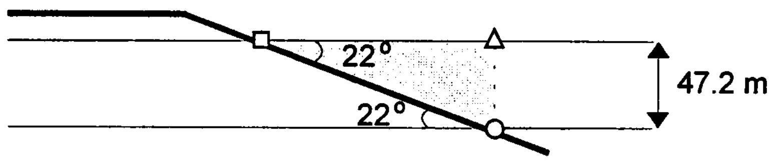

b.

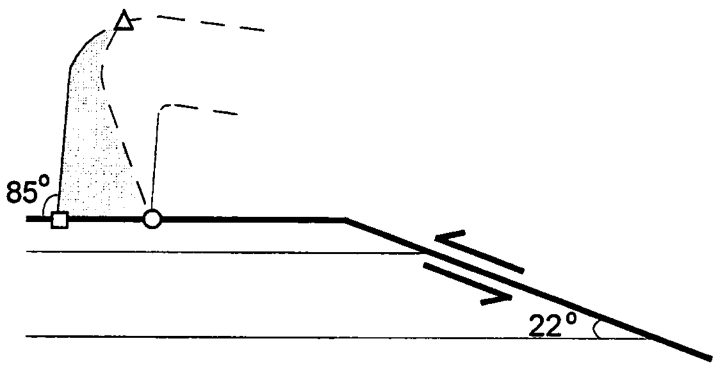

of 1.1 for flexural flow with a strain ratio of 3.0 and θ" of 32°. These values are smaller than those for fault-bend folding and folding-after-fault propagation because less limb rotation would occur during folding. If buckling occurred through tangential longitudinal strain instead, the main anticlinal hinge sustains a bending strain in which outer-arc extension is 66% and inner-arc contraction is 40% (Figure 5d). These types of deformation allow the main hinge to be pinned during folding prior to break-thrusting (Mitchell & Woodward 1988, Fischer *et al.* 1992), unlike fault-bend folding or folding-after-fault propagation. In addition, the fold would record an overprint during passage through the upper fault bend similar to the overprint recorded when fault propagation precedes folding. This strain could consist of 20 percent shortening, which produces a strain ratio of 1.6. For example, the strain could be recognized as extensional structures that record a bulk deformation and deformed earlier synfolding structures.

MESOSTRUCTURES

Mesoscale structures in the Tuscarora Sandstone in the study area include bedding-parallel slip surfaces, contraction faults, and extensional cataclastic bands and veins (Figure 7; Tables B.1, B.2). The mesostructures are heterogeneously distributed throughout the southern and northern profiles (Figures 8 and 9). The forelimb and main hinge contain most of the mesoscale deformation, whereas the backlimb exhibits few mesostructures and the footwall exhibits none.

The forelimb and hinge in the southern profile are well exposed. One location in the outer arc of the forelimb at station S1 (Figures 8a, A.2) contains one set of quartz veins subparallel to bedding strike and subperpendicular to bedding dip, with widths of less than 1 mm. Sixteen of these veins in 50 cm of outcrop provide a total extension of 0.5-1.0%. Oriented as they are relative to bedding, these veins may reflect outer-arc extension from flexural folding. An adjacent location (station S2) contains two sets of systematically oriented veins, all of which have at least a vuggy quartz fill. One vein set exploits cross-bedding. The second set of veins, oriented normal to bedding strike and at a high angle to bedding dip, consists of fifteen veins in 50 cm of exposure. Their orientation normal to the first set suggests a second extensional event, in addition to that from flexural folding. These vein sets do not occur together, however, so no age relationship could be determined. Additionally, restricted occurrence of these structures indicates only localized extension.

Pervasive cataclastic bands (Lloyd & Knipe 1992, Onasch & Dunne 1993) occur in the basal pebble conglomerate of the inner-arc forelimb and hinge

Figure 7. Representative mesostructures in study area. (a) Cataclastic bands in basal pebble conglomerate of southern hinge at station S9. (b) Fracturing in northern hinge at station N17. Approximate bedding orientation is indicated by yellow lines. Length of photo represents approximately 5 meters. (c) Veins in northern backlimb at station N3.

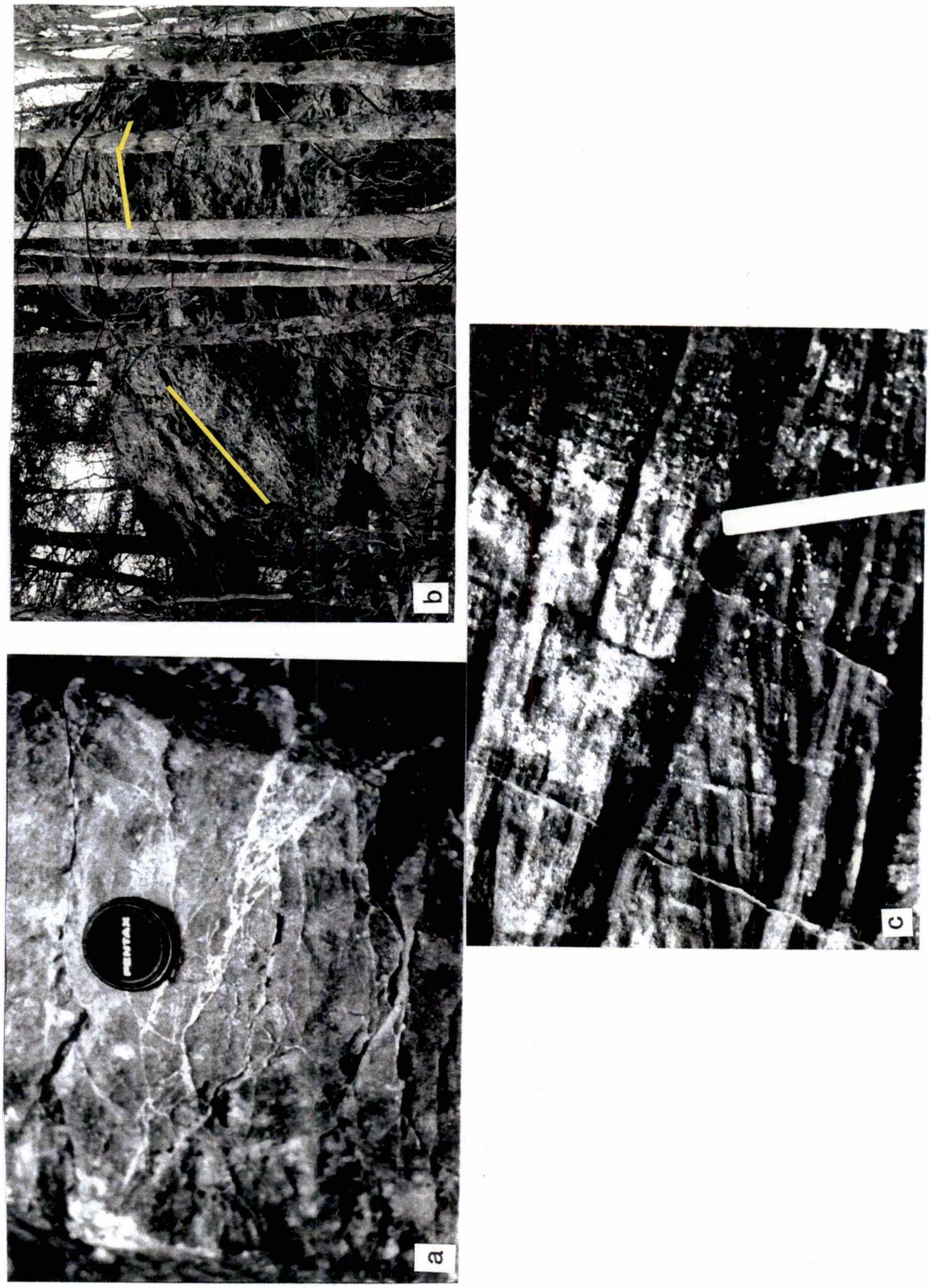
b
a
c

Figure 8. Mesostructural distributions for the south profile (B-B'). Locations of: a) veins, (b) faults (associated with cataclastic bands in the basal pebble conglomerate of the inner-arc forelimb and hinge), and (c) bedding-parallel slip. Dots indicate locations of sample stations.

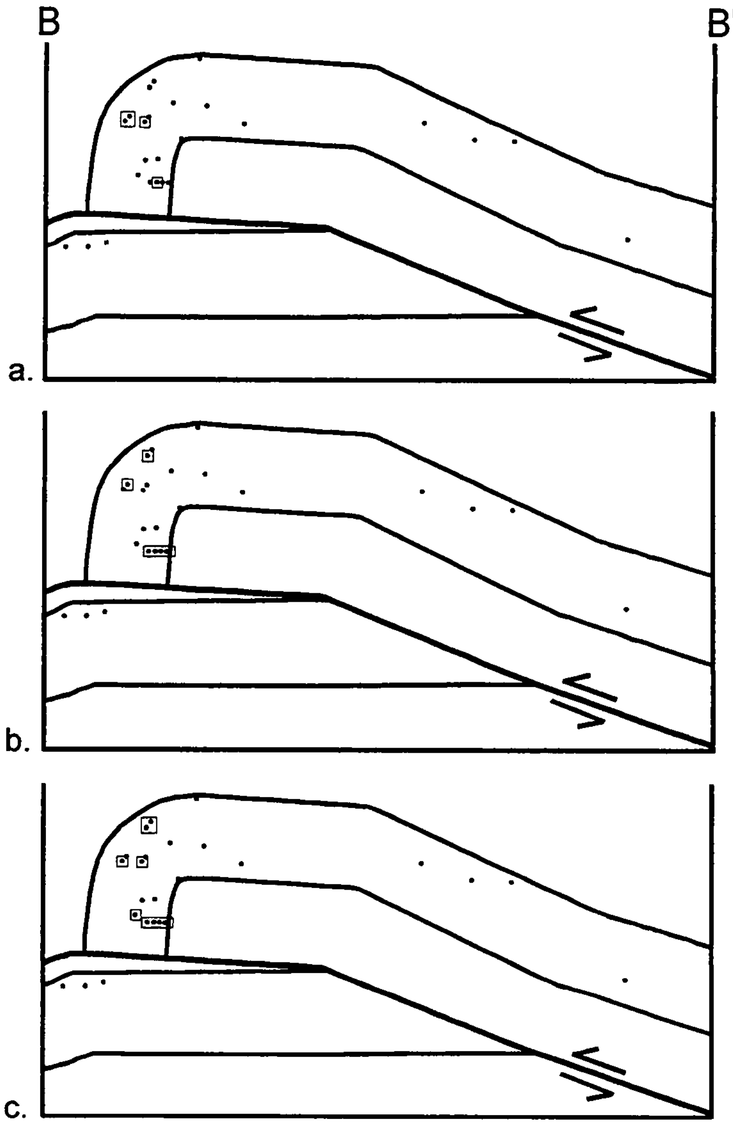
B
B'
a.
b.
c.

Figure 9. Mesostructural distributions for the north profile (A-A'). Locations of: (a) bedding-parallel slip, (b) veins, and (c) faults. Dots indicate locations of sample stations.

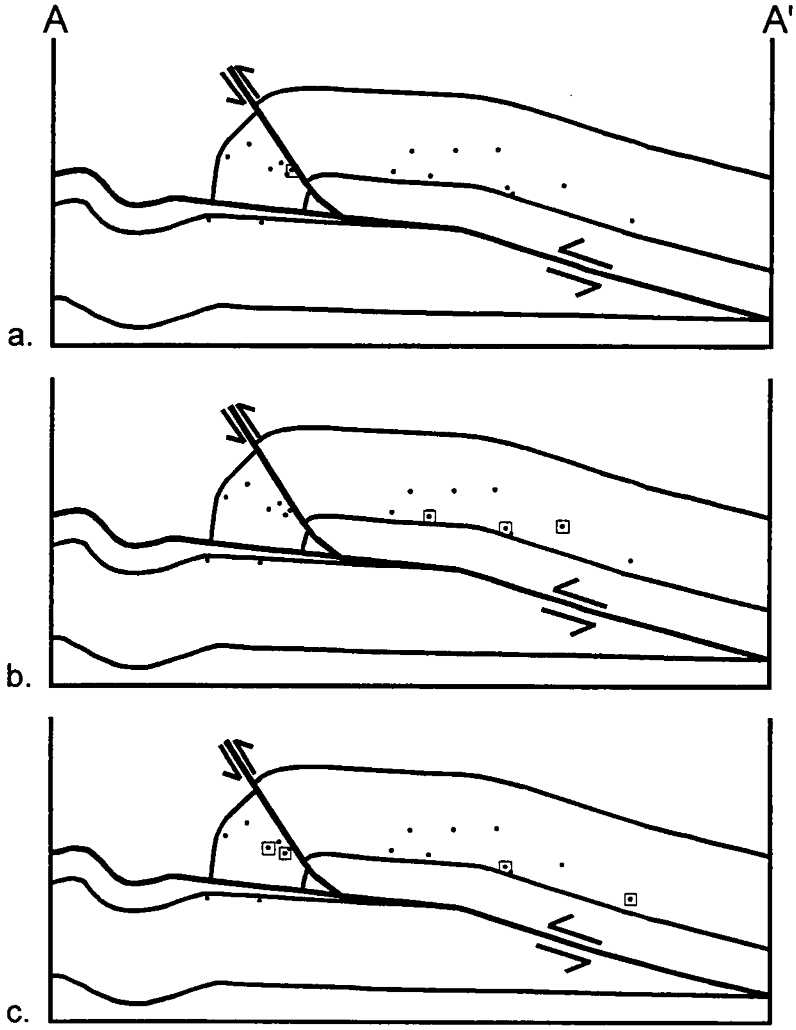
A
A'
a.
b.
c.

(Figure 7a). They contractionally offset pebbles across surfaces ornamented with slickenlines (Figure 8b). Forty-seven such bands occur in the 6 m of the Tuscarora Sandstone at stations S9-S11. Although average band spacing is 3.4 cm, their frequency decreases to zero at 6 m above the base, so that no cataclastic bands occur in the overlying massive quartz arenite. Most bands have displacements of 0.5 mm or less, and widths of 1 mm or less. Displacement does not correlate to band width, because the bands wider than 1 mm also displaced less than 0.5 mm.

The southern forelimb and hinge contain other slip surfaces. One contraction fault, located at station S2 in the outer forelimb near the hinge (Figure 8b), is oriented normal to bedding strike, has a 5-m trace length across the outcrop, and displaces four medium-thickness beds by 9 cm. Bedding-parallel slip surfaces occur in both the forelimb and hinge at stations S1, S3, S9 to S13, S16, and S17 (Figure 8c). In the outer arc of the hinge at station S3, slip surfaces occur at 1.5-m intervals. In the forelimb at stations S9-S13, there are 9 bedding-parallel slip surfaces in 16.2 m of stratigraphic section. The lower 3.6 m contains 3 slip surfaces, the next 7.4 m contains only one slip surface, and the upper 5 m contains 5 slip surfaces. These surfaces are interpreted to indicate abundant layer-parallel slip in the forelimb and hinge during folding.

In contrast to the southern profile, the forelimb and hinge in the northern profile are poorly exposed. No bedding-parallel slip surfaces are visible in the north forelimb (Figure 9a). However, at sites within 1 km of the study area, steeply dipping Tuscarora Sandstone layers always provide abundant evidence for bedding-parallel slip. Thus, the absence of slip surfaces in the north forelimb may only be an artifact of poor exposure.

Fracturing dominates the inner arc of the northern hinge at stations N16 and N17 (Figure 7b). There are at least 4 systematic fracture sets: one set is subhorizontal, the second is subvertical on a strike of 035, the third is inclined to the NW at about 13°, and the fourth is subvertical, trending 115 and dipping steeply to the SW. This pervasive fracturing imparts a blocky texture to the sandstone, with individual blocks measuring 2-3 cm in length on each side. The frequency of fracturing is greater in the inner arc of the hinge than anywhere else in the structure, and the intensity of fracturing decreases greatly in the 10 m across bedding, from the inner arc (highest) to the outer arc (almost none). Many fracture surfaces have contractionally faulted and exhibit slickenlines. This discrete structural suite in the northern hinge does not occur in any other domain, north or south.

The hinge-localized fractures in the northern exposure of the anticline contrast with the more uniform distribution of faults and bedding-parallel slip surfaces in the southern hinge and forelimb. This contrast could result from a difference in hinge deformation during fold amplification. A major factor in controlling the development and distribution of hinge-related structures is the role of hinge migration during folding (Williams 1979, Gray 1981, Mitchell & Woodward 1988, Suppe 1985, Fischer *et al.* 1992). For example, a rock layer undergoing tangential longitudinal strain has deformation concentrated in the hinge zone (Ramsay 1967). If the hinge is fixed during fold amplification, precluding migration, this deformation produces a suite of structures unique to the hinge and absent in either fold limb (Mitchell & Woodward 1988, Fischer *et al.* 1992). If the hinge migrates during folding, however, a similar suite of structures would be found in both the hinge and at least one fold limb. Rocks deformed in the hinge would pass to a limb during migration and carry the hinge structures as a older imprint (Williams 1979, Gray 1981, Fischer *et al.* 1992).

The southern hinge lacks the localized pervasive fracturing of the northern hinge, but it contains mesostructures, such as cataclastic bands and bedding-parallel slip, that are present in the adjacent forelimb. This distribution of mesostructures is interpreted to result from migration of the southern hinge during fold development (Fischer *et al.* 1992). Along strike to the north, however, the mesostructures are heterogeneously concentrated in the hinge. This distribution is interpreted to result from fixed-hinge folding.

An explanation for this difference in hinge behavior between the northern and southern locations is the presence of an imbricate thrust adjacent to the northern hinge (Figure 3). This thrust has 6 m of stratigraphic throw and is interpreted to have formed coevally with folding (Figure 4). During folding, the fault was an active surface adjacent to the anticlinal core that prevented migration of rock through the hinge, thereby fixing it. Conversely, the absence of this imbricate to the south may have allowed hinge migration in the core.

The flat-and-ramp portions of the southern backlimb exhibit no mesostructures, possibly as a result of the paucity of exposures there. In contrast, northern backlimb domains are well exposed. The flat portion of the northern backlimb lacks mesostructures, except for a set of veins at station N3 in the lower portion of the Tuscarora Sandstone (Figures 7c, 9b). Seven veins occupy a one-meter length of outcrop, strike normal to bedding strike, and dip normal to bedding. They are 3 to 4 mm in width, resulting in a local extension of only 0.3-0.4%.

The backlimb above the footwall ramp contains a few localized systematic vein sets at stations N2 and N8 (Figure 9b) that may be related to faulting. A few contractional faults at stations N1 and N2 occur at low angles to bedding, and other faults exploit cross bedding (Figure 9c). The faults strike either parallel or perpendicular to bedding strike. Most displacements are less than 1 cm, with one exception of 57 cm. All of the faults have 1 to 4 mm zones of solid to anastomosing quartz fill. If the Barclay thrust acted as a neutral surface for the fault bends (Figure 3) (Wiltschko 1979, Wiltschko *et al.* 1985), rock passage through the lower fault bend would cause layer-parallel contraction, and the minor contraction faults may have formed then. Alternatively, these faults may have formed during layer-parallel shortening. The latter scenario is less likely, because regional layer-parallel shortening should produce faults at this stratigraphic level throughout the study area, which is not the case.

MICROSTRUCTURES

Types of microstructures

The bedding-perpendicular, strike-perpendicular thin section of each sample was point-counted for 250 microstructures (Appendix C). These microstructures included those resulting from dislocation glide, microfracturing, and pressure solution. Dislocation flow produces such intragranular features as undulatory extinction, deformation lamellae, and deformation bands (Groshong 1988). Undulatory extinction is identified in this study by sweeping extinction patterns in quartz grains. Deformation lamellae consist of parallel sets of narrow lines possessing different refractive indices from the host grain (Figure 10a) (Groshong 1988). Deformation bands are distinct bands with different crystallographic orientations than the host grain (Figure 10b) (Groshong 1988). They range from 0.01 to 0.1 mm in width (Onasch & Dunne 1993).

Microfracturing produces structures that include fluid inclusion planes, microveins, and cataclastic bands. Fluid inclusion planes, or FIPs, are healed microfractures containing fluid inclusions characteristically 1 to 10 μm in diameter (Figure 10a) (Onasch & Dunne 1993). In the Tuscarora Sandstone samples examined for this study, FIPs are both intragranular and transgranular features. Where they are transgranular, FIPs commonly occur in sets. These sets are only locally abundant at the microscale but have a fracture spacing of 0.01 to 0.03 mm. Microveins are transgranular features filled with quartz and have widths of 0.01 to 0.20 mm (Figure 10c,d). They exist in optical continuity with adjacent grains in transmitted light, but in cathodoluminescence they produce a dull luminescence and contrast with the blue and pink luminescence

Figure 10. Photomicrographs of microstructures: (a) deformation lamellae (DL) and fluid inclusion planes (FIP) viewed under crossed polarizers;
(b) deformation bands (DB) viewed under crossed polarizers; (c) microvein (MV) viewed under cathodoluminescence ; (d) same view as in (c), but viewed under crossed-polarizers.

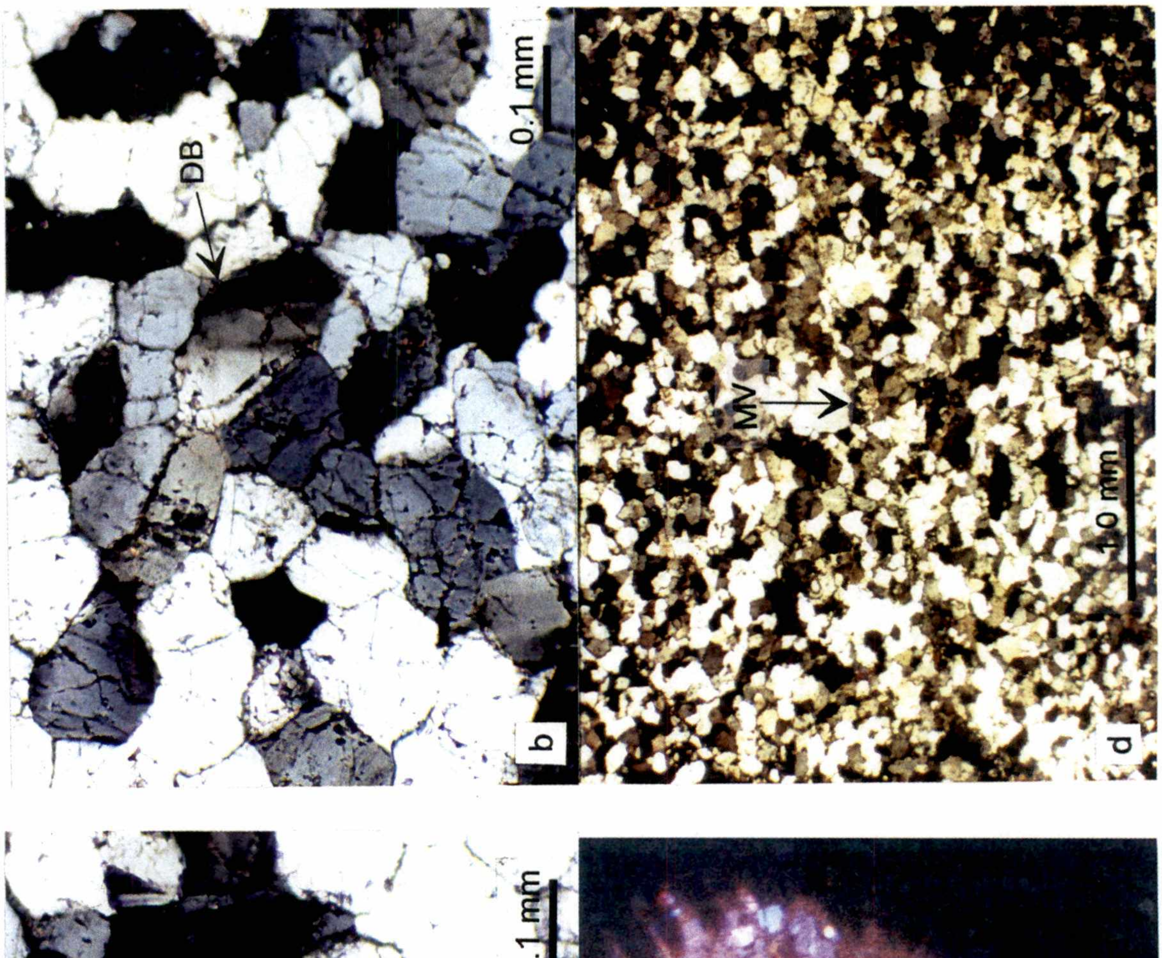
a
FIP
DL
0.1 mm
b
DB
0.1 mm
c
MV
1.0 mm
d
MV
1.0 mm

of the detrital quartz grains (Houseknecht 1988, Onasch 1990). Cataclastic bands, another transgranular feature, consist of subplanar zones of fine-grained, poorly sorted angular quartz that offset adjacent quartz grains.

Microstructures related to pressure solution include transgranular stylolites and interpenetrated grain boundaries resulting from grain-to-grain solution. The interpenetrated grains were not point-counted because they are only visible in cathodoluminescence, and the point-counting device could not be used with the cathodoluminescent stage. Cathodoluminescence causes detrital quartz grains to luminesce pink and blue, which distinguishes them from brown-luminescing quartz overgrowths and reveals any grain interpenetration. Consequently, grain-to-grain solution was measured separately using the pressure-solution strain (PSS) method (Onasch 1994), which will be discussed later.

Microstructural abundances

Microstructures were point-counted in the bedding- and strike-perpendicular ("v") sections of all samples (Appendixes A, C). These abundances were tabulated for the five structural domains of each profile and for each entire profile (Figure 11). Undulatory extinction is the most common feature in all domains and is equally abundant in all domains. Undulatory extinction in quartz grains of the Tuscarora Sandstone could be inherited by deposition from metamorphic source rocks, rather than being related to the formation of the Barclay anticline and thrust (Dorsch 1993, Onasch & Dunne 1993). However, other dislocation-related structures, such as deformation bands and deformation lamellae, are evenly distributed through all domains

Figure 11. Microstructural abundance charts: (a) forelimb, (b) hinge, (c) backlimb (above the roof flat), (d) backlimb (above the thrust ramp), (e) footwall, and (f) all five structural domains of the cross sections A-A' (north) and B-B' (south) of Figure 3. Dark gray bars represent values for the north profile and light gray bars represent values for the south profile.

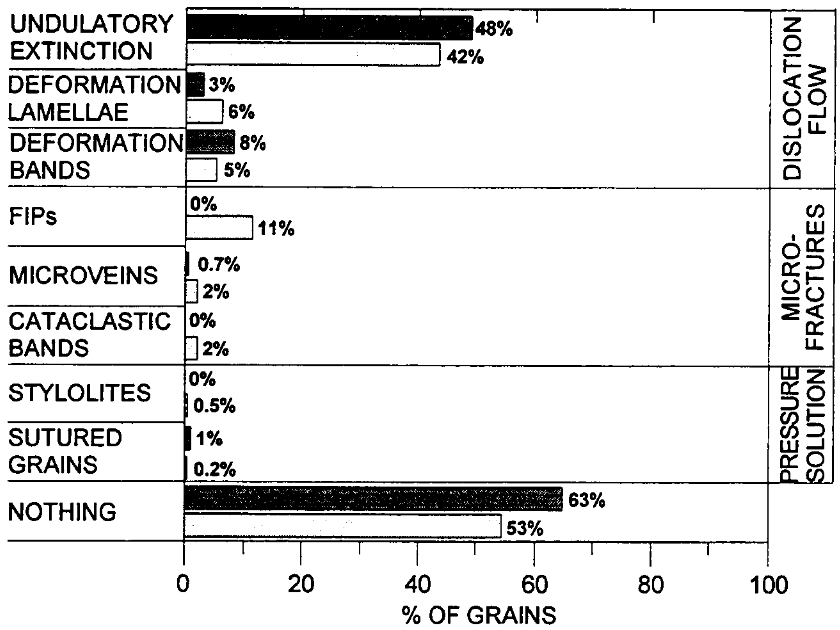

UNDULATORY EXTINCTION
48%
42%
DEFORMATION LAMELLAE
3%
6%
DEFORMATION BANDS
8%
5%
FIPs
0%
11%
MICROVEINS
0.7%
2%
CATACLASTIC BANDS
0%
2%
STYLOLITES
0%
0.5%
SUTURED GRAINS
1%
0.2%
NOTHING
63%
53%
DISLOCATION FLOW
MICRO-FRACTURES
PRESSURE SOLUTION
0
20
40
60
80
100
% OF GRAINS

a.

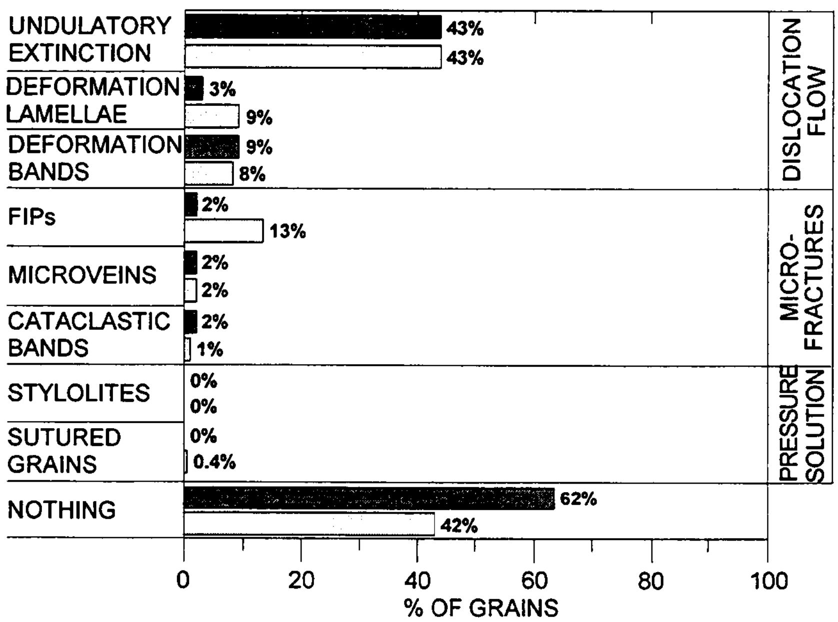

UNDULATORY EXTINCTION
43%
43%
DEFORMATION LAMELLAE
3%
9%
DEFORMATION BANDS
9%
8%
FIPs
2%
13%
MICROVEINS
2%
2%
CATACLASTIC BANDS
2%
1%
STYLOLITES
0%
0%
SUTURED GRAINS
0%
0.4%
NOTHING
62%
42%
DISLOCATION FLOW
MICRO-FRACTURES
PRESSURE SOLUTION
0
20
40
60
80
100
% OF GRAINS

b.

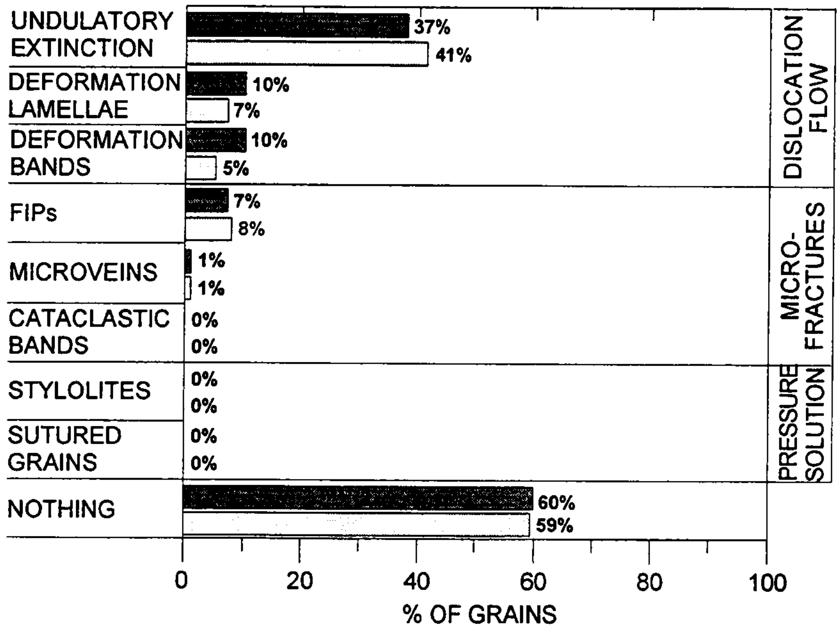
UNDULATORY EXTINCTION
37%
41%
DEFORMATION LAMELLAE
10%
7%
DEFORMATION BANDS
10%
5%
FIPs
7%
8%
MICROVEINS
1%
1%
CATACLASTIC BANDS
0%
0%
STYLOLITES
0%
0%
SUTURED GRAINS
0%
0%
NOTHING
60%
59%
DISLOCATION FLOW
MICRO-FRACTURES
PRESSURE SOLUTION
0
20
40
60
80
100
% OF GRAINS

c.

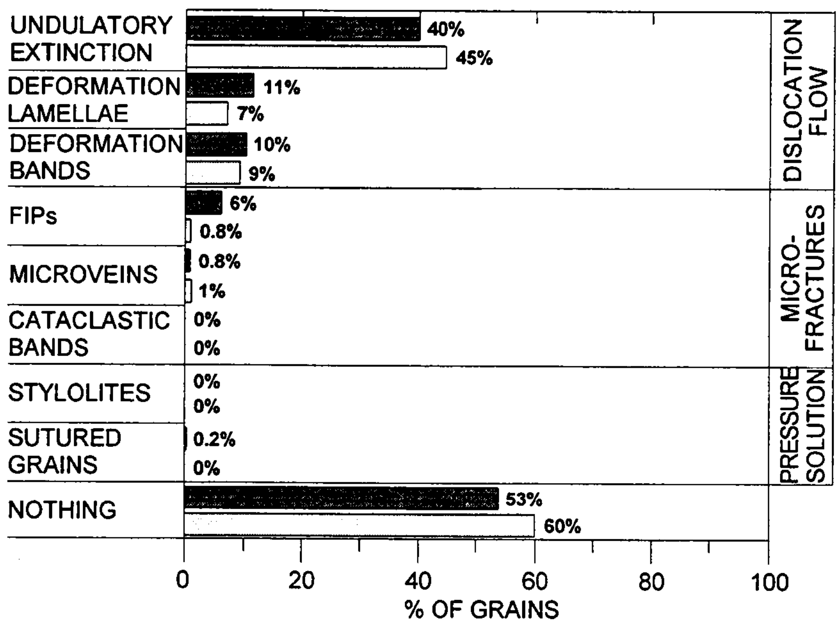
UNDULATORY EXTINCTION
40%
45%
DEFORMATION LAMELLAE
11%
7%
DEFORMATION BANDS
10%
9%
FIPs
6%
0.8%
MICROVEINS
0.8%
1%
CATACLASTIC BANDS
0%
0%
STYLOLITES
0%
0%
SUTURED GRAINS
0.2%
0%
NOTHING
53%
60%
DISLOCATION FLOW
MICRO-FRACTURES
PRESSURE SOLUTION
0
20
40
60
80
100
% OF GRAINS

d.

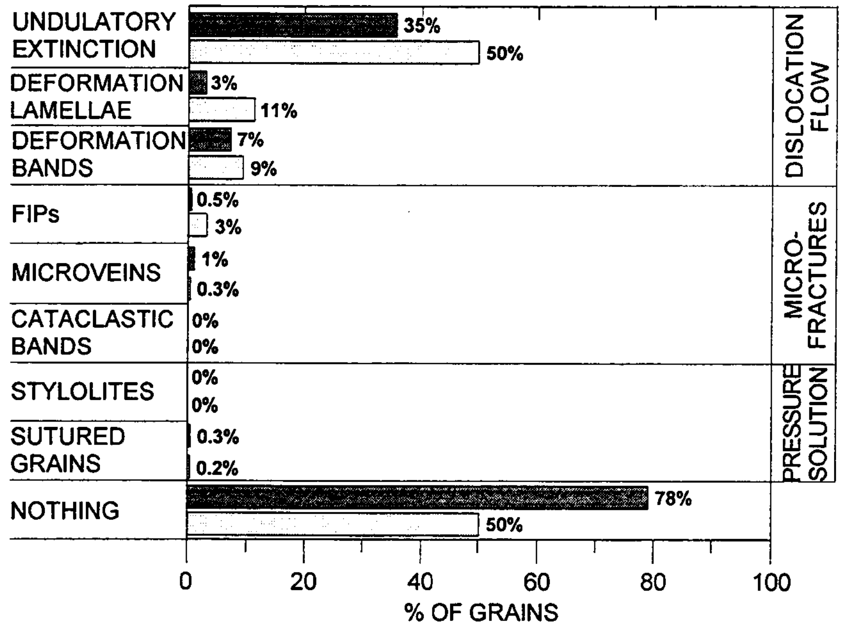
UNDULATORY EXTINCTION
35%
50%
DEFORMATION LAMELLAE
3%
11%
DEFORMATION BANDS
7%
9%
FIPs
0.5%
3%
MICROVEINS
1%
0.3%
CATACLASTIC BANDS
0%
0%
STYLOLITES
0%
0%
SUTURED GRAINS
0.3%
0.2%
NOTHING
78%
50%
DISLOCATION FLOW
MICRO-FRACTURES
PRESSURE SOLUTION
0
20
40
60
80
100
% OF GRAINS

e.

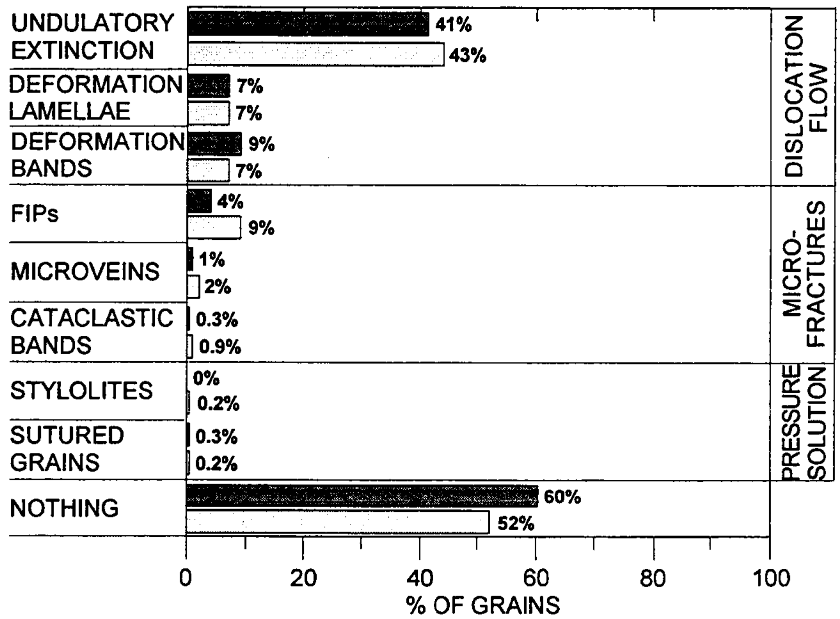
UNDULATORY EXTINCTION
41%
43%
DEFORMATION LAMELLAE
7%
7%
DEFORMATION BANDS
9%
7%
FIPs
4%
9%
MICROVEINS
1%
2%
CATACLASTIC BANDS
0.3%
0.9%
STYLOLITES
0%
0.2%
SUTURED GRAINS
0.3%
0.2%
NOTHING
60%
52%
DISLOCATION FLOW
MICRO-FRACTURES
PRESSURE SOLUTION
0
20
40
60
80
100
% OF GRAINS

f.

(Figure 11). These structures have been shown to deform both detrital grains and cement in the Tuscarora Sandstone, implying that they are not inherited (Onasch & Dunne 1993). The uniform abundances of all dislocation-related microstructures is interpreted to indicate that dislocation-related deformation was not inherited and represents a uniform deformation across the study area. In this region, the most likely cause for such uniform deformation is layer-parallel shortening prior to folding (Geiser 1974, Dean *et al.* 1988, Ferrill & Dunne 1989).

Fluid inclusion planes represent 1 to 13% of the grains in most domains, and are less common in the footwall than in the hanging wall. Microveins and cataclastic bands are restricted to less than 2% of the grains in any domain. Cataclastic bands, including those at outcrop scale, form only in the conglomerate at the base of the Tuscarora Sandstone, which indicates that cataclasis is a deformation behavior restricted to the coarser-grained quartz-rich lithologies. Stylolites are rare, implying that development of solution-related discontinuities across bedding is uncommon.

Extensional strains from microveins (Table 3) (Onasch 1990) were determined for the ten samples that contained the most microveins (Tables C.1, C.2). Microvein widths were measured across thin sections normal to fracture orientation. Extensions range from 0.2 to 4.1% for each microvein set, with all but one set containing less than 2.7% extension. Microvein formation is a dilational event (Onasch 1990), so that extensional strains are equivalent to volume increases. Summing the strains for each sample, extensions are greater in the hinge and forelimb than in the backlimb (2.7 to 9.4% vs. 1 to 3.2%). A possible cause for this difference is that some forelimb and hinge samples (N13, S2, S3, S16, and S17) are located in the outer-arc of the anticline, and would have experienced outer-

Table 3. Microvein extensional strains (expressed as percentages).

		Bedding-parallel section			Bedding- and dip-perpendicular section			Bedding-perpendicular, dip-parallel section		
Sample	Domain	Strike-parallel	Strike-perp.	Strike-oblique	Bed-parallel	Bed-perp.	Bed-oblique	Bed-parallel	Bed-perp.	Bed-oblique
b-N5	Backlimb:	0.4								
p-N5	flat					2.4				
v-N5								0.4	.	
b-N13				2.6						
p-N13	Forelimb				0.5		1.2			
v-N13									0.6	2.2
b-N17			0.4	2.2						
p-N17	Hinge				0.7		1.7			
v-N17								0.2	3.5	0.7
b-S2				1.6						
p-S2	Forelimb				0.5	0.5	2.0			
v-S2										0.6
b-S3		1.8	1.1	0.6						
p-S3	Forelimb					0.4	3.1			
v-S3										2.4
b-S7	Backlimb:			0.2						
p-S7	flat						0.2			
v-S7										0.6
b-S10				0.8						
p-S10	Forelimb					1.4				
v-S10										1.4
b-S12				1.2						
p-S12	Forelimb						2.2			
v-S12								0.3	4.1	0.4
b-S16				2.6						
p-S16	Hinge						0.3			
v-S16										2.6
b-S17				0.8						
p-S17	Hinge						1.0			
v-S17										0.9

arc extension. The significant extensional strain in the two southern forelimb samples (S10 and S12) is consistent with the other deformation of the pebble conglomerate in the forelimb and hinge, such as cataclastic bands and FIPs. Because other samples from Tuscarora Sandstone contain fewer microveins than the measured samples, the bulk dilation in the Tuscarora Sandstone from microveins is quite small.

Microstructural occurrences

Microstructural occurrences were statistically correlated. A *t*-test was performed on correlations determined by linear regression (Table 4). Some pairs of microstructures were shown to have a non-random association. The most significant correlation is that between microveins and cataclastic bands, which reflects the fact that cataclastic bands are always observed with microveins. Among the dislocation-related mechanisms, the correlation is statistically significant and positive between deformation lamellae and deformation bands, as well as between undulatory extinction and deformation bands. Such a correlation is consistent with their abundance in all fold domains. Certain microstructures that result from different mechanisms also positively correlate. For example, subgrains are commonly found adjacent to fracture-related microstructures, but not dislocation-related structures. This correlation may reflect discrete lattice reorientation within grains by fracturing, as opposed to dislocation accumulation.

Microstructural occurrences vary little between the north and south profiles within the same domain (Figure 11). This consistency suggests that similar deformation mechanisms were active in a given domain along structural

Table 4. Microstructural correlation data. Bold-faced values are significant at the 95% confidence level (r = 0.26).

	Undulatory Extinction	Subgrains	Deformation Lamellae	Deformation Bands	FIPs	Microveins	Cataclastic Bands	Stylolites	Sutured Grains
Und. Ext.	1.00								
Subgrains	0.20	1.00							
Def. Lam.	0.16	0.18	1.00						
Def. Bands	**0.30**	-0.21	**0.46**	1.00					
FIPs	-0.06	**0.50**	**0.31**	-0.16	1.00				
Microveins	0.03	**0.40**	0.03	-0.10	0.18	1.00			
Cat. Bands	0.06	**0.40**	-0.05	-0.18	**0.28**	**0.75**	1.00		
Stylolites	-0.08	0.15	-0.15	**-0.33**	**0.29**	-0.04	-0.08	1.00	
Sut. Grains	0.10	0.05	-0.15	0.10	-0.08	-0.12	-0.12	0.25	1.00

trend. Fluid inclusion planes and microveins exist in greatest concentrations in the forelimb and hinge. Cataclastic bands are present only in the conglomeratic base of the Tuscarora Sandstone in the inner arc of the main fold and forelimb. They are a microscale effect of the abundant contraction faults in this interval.

Relative ages of microstructures

Fluid inclusion planes are only locally abundant. Where present they are so sparse as to provide little information about age relationships. A few samples from the forelimb of the south profile contain microveins with parallel FIPs, which suggests that the two structures formed at the same time (Onasch 1990).

The south and north forelimbs and hinges contain abundant microfractures in the form of microveins and cataclastic bands. The microveins and cataclastic bands consistently crosscut interpenetrated grains, indicating that grain-to-grain pressure solution occurred before fracturing.

Many samples contain only one set of microveins that share the same orientation. Some samples contain more than one microvein set, with sets oriented obliquely to each other in most cases. None of these samples exhibit offset of one type of microvein by another, suggesting that most veins formed at the same time.

The grains comprising microvein fill generally contain undulatory extinction, and in a few veins they contain deformation lamellae and deformation bands. These dislocation-related structures may have been inherited as the grains grew from the wallrock into the fracture. Alternatively, these structures may have overprinted earlier extension structures.

GRAIN-TO-GRAIN SOLUTION

Methodology

Volume loss due to grain-to-grain solution was determined for a representative sample set using a new pressure-solution strain (PSS) method (Onasch 1993, Onasch 1994). The method involves reconstructing the original grain boundaries of interpenetrated quartz grains (Figure 12) from cathodoluminescent photomicrographs and estimating the amount of "overlap quartz" (Houseknecht 1988, Onasch 1993). Strain is then determined from the amounts of interpenetration and orientations of the straight-line compromise boundaries.

Only 20 samples were analyzed (Table 5, Appendix D) because the PSS method is quite time consuming. Measurement areas in photomicrographs were chosen that lack transgranular heterogeneous structures, such as microveins, to preserve homogeneity during analysis. Measured pressure-solution strains are conservative estimates because: (1) they were made only where grains clearly indent other grains, so straight boundaries that might contribute significant solution were ignored; (2) indenters were treated as rigid bodies, but their amplitudes may have been reduced during solution; (3) only interpenetrations between original grains are measured, so any solution of diagenetic cements is ignored (Dunne & Caldanaro *in review*).

Strain magnitudes

Strain ellipses for the PSS data were measured in three mutually perpendicular planes (Table 5) and ellipsoids were calculated from the ellipses (Table D.1) (Owens 1984). The R_{xy} and R_{yz} strain ratios are small, with

Figure 12. Photomicrographs of grain-to-grain solution. (a) CL photomicrograph of grain-to-grain interpenetrations with original grain boundaries noted in red. (b) Same view as in (a), but under crossed polarizers. Interpenetrated grain pairs are identified by numbers.

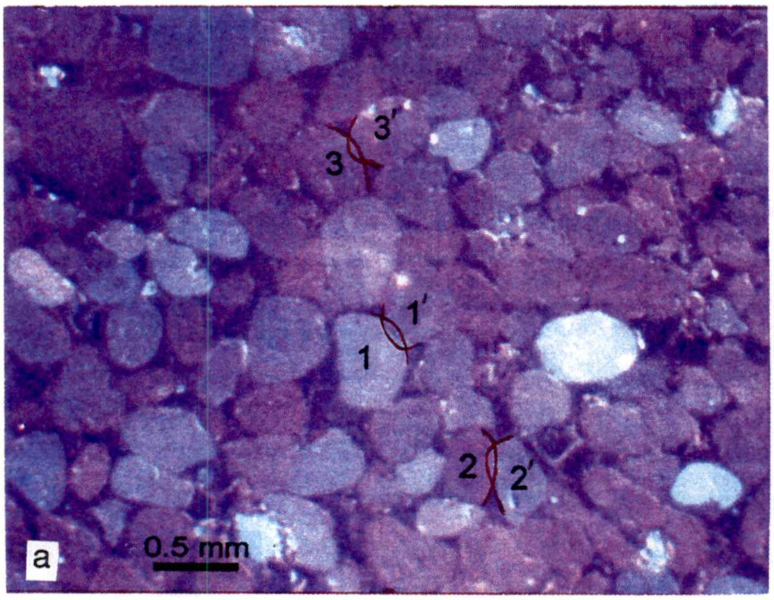
3
3′
1
1′
2
2′
a
0.5 mm

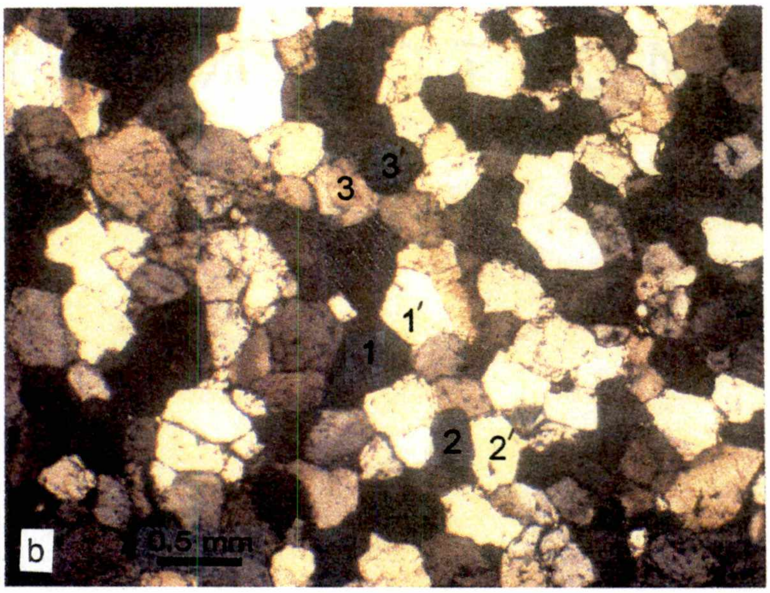
3
3′
1′
1
2
2′
b
0.5 mm

Table 5. Strain ellipses measured with the PSS method.

	b-section					p-section					v-section					Total
Sample	Long axis	Short axis	Axial ratio	Axial rake	% Area loss	Long axis	Short axis	Axial ratio	Axial rake	% Area loss	Long axis	Short axis	Axial ratio	Axial rake	% Area loss	% Volume Loss
N1	0.84	0.78	1.08	136	34	0.82	0.79	1.04	137	35	0.86	0.85	1.01	0	27	
N2	0.84	0.83	1.01	139	30	0.80	0.77	1.04	19	38	0.85	0.83	1.02	90	29	
N3	0.84	0.82	1.02	90	31	0.80	0.76	1.05	90	39	0.85	0.81	1.05	0	31	-35
N7	0.81	0.81	1.00	0	34	0.84	0.82	1.02	90	31	0.86	0.85	1.01	90	27	-30
N9	0.87	0.87	1.00	0	24	0.88	0.86	1.02	0	24	0.90	0.87	1.03	33	22	
N12	0.87	0.85	1.02	0	26	0.87	0.85	1.02	0	26	0.85	0.83	1.02	90	29	-29
N13	0.87	0.85	1.02	0	26	0.85	0.85	1.00	0	28	0.85	0.85	1.00	0	28	-28
N14	0.89	0.86	1.03	0	23	0.89	0.86	1.03	0	23	0.88	0.87	1.01	0	23	-24
N16	0.86	0.85	1.01	0	27	0.87	0.85	1.02	0	26	0.87	0.85	1.02	0	26	-27
FN1	0.86	0.78	1.10	0	33	0.87	0.85	1.02	0	26	0.85	0.83	1.02	90	29	-32
S2	0.87	0.83	1.05	90	28	0.85	0.85	1.00	0	28	0.91	0.85	1.07	0	23	-26
S5	0.89	0.88	1.01	90	22	0.86	0.84	1.02	0	28	0.88	0.88	1.00	0	23	-24
S7	0.89	0.87	1.02	90	23	0.90	0.88	1.02	90	21	0.92	0.87	1.06	153	20	
S9	0.91	0.85	1.07	128	23	0.90	0.86	1.05	0	23	0.90	0.86	1.05	0	23	
S12	0.87	0.86	1.01	0	25	0.87	0.86	1.01	0	25	0.87	0.85	1.02	0	26	-26
S14	0.88	0.86	1.02	0	24	0.88	0.86	1.02	90	24	0.88	0.84	1.05	0	26	-27
S16	0.87	0.86	1.01	0	25	0.88	0.85	1.04	41	25	0.88	0.85	1.04	90	25	
S19	0.87	0.87	1.00	0	24	0.88	0.87	1.01	132	23	0.87	0.85	1.02	0	26	
S22	0.88	0.87	1.01	0	23	0.90	0.87	1.03	0	22	0.87	0.86	1.01	90	25	-25
FS1	0.89	0.81	1.10	137	28	0.86	0.82	1.05	0	29	0.86	0.84	1.02	0	28	-31

Rake measured in the plane of bedding with strike as a common reference frame.

most less than 1.05 (Table D.1; Figure 13). Although the resulting ellipsoids are nearly spherical, the elongations remain significant, with most ranging from 10-20%. Consequently, average area loss is 27% per thin section and average volume loss per sample is 28±3% by solution (Table 5). The average volume loss of 28% from PSS is greater than the combined rock porosity (<1%), average amount of preserved diagenetic cement (6%) (Table 6), and volume increases related to dilation from microvein formation (≤3% in any direction). Therefore, the Tuscarora Sandstone underwent net volume loss during both lithification and tectonism.

Strain orientations

PSS ellipsoid axis orientations are depicted in equal-area stereonets in which bedding was rotated to the horizontal (Figure 14). Restoring bedding to the horizontal provides a common reference plane for the samples in the stereonets. The restoration was selected because quartz-rich sandstones commonly record a bedding-normal syndiagenetic compaction (Pettijohn *et al.* 1987, Houseknecht 1988), and therefore bedding would be a useful reference state as the equatorial plane for the stereonets. The PSS ellipsoid axes for the Tuscarora Sandstone display no polar or girdle distributions (Figure 14). The lack of preferred orientation for the strain axes reflects the nearly spherical ellipsoid shapes, but is unexpected.

Interpretation of PSS data

Quartz-cemented sandstones are known to undergo significant diagenetic compaction (Pettijohn *et al.* 1987, Houseknecht 1988, Couzens *et al.* 1993,

Figure 13. Flinn plot of pressure solution strain data (20 samples).

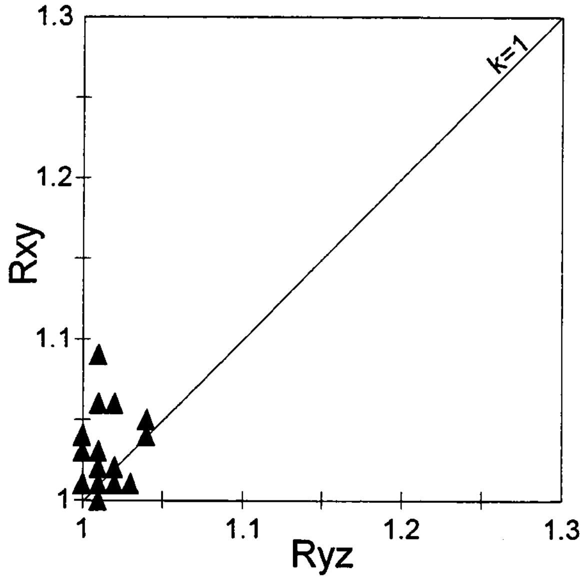
1.3
1.2
1.1
1
Rxy
k=1
1
1.1
1.2
1.3
Ryz

Table 6. Percentage of silica cement in quartz arenite samples.

Sample	% of 200 grains
N1	4
N2	9.5
N3	3.5
N4	2
N5	2
N6	3
N7	4.5
N8	6
N9	1.5
N12	7.5
N13	6
N14	4
N15	5
N16	3
N17	3
FN1	9.5
FN2	12
S1	7.5
S2	6
S3	8
S4	3.5
S5	4.5
S6	4
S7	4.5
S8	13
S9	2
S10	7
S11	3.5
S12	5
S13	5
S14	6
S15	5
S16	8.5
S17	3.5
S18	4.5
S19	4.5
S20	8.5
S22	7.5
FS1	5
FS2	7.5
FS3	10

Figure 14. Equal-area lower hemisphere projections depicting PSS incremental strain ellipsoid axial orientations. Bedding is restored to horizontal to provide a common plane of reference.

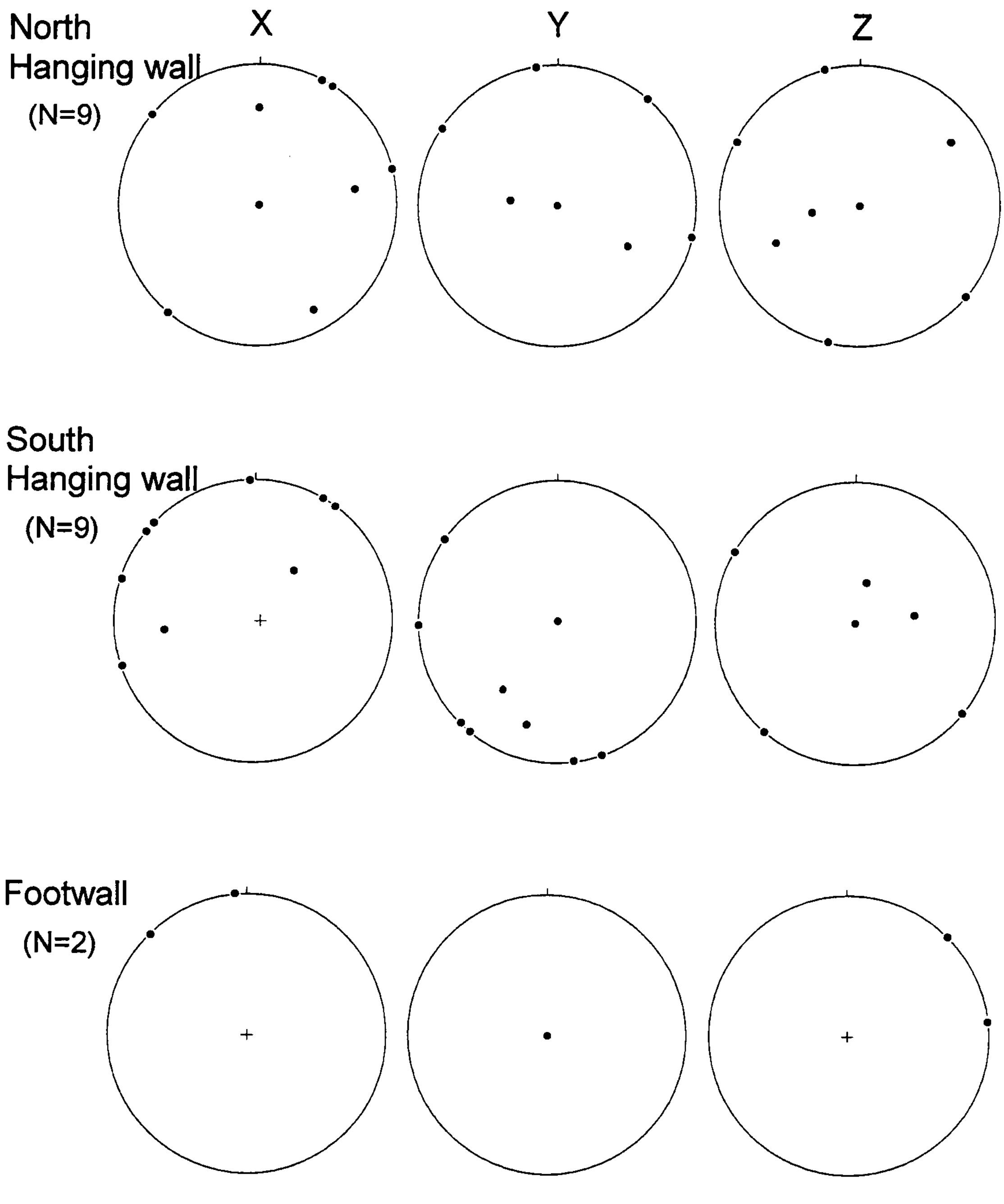

X
Y
Z
North
Hanging wall
(N=9)
South
Hanging wall
(N=9)
Footwall
(N=2)

Onasch & Dunne 1993). It is also known that grain-to-grain solution is a significant contributor to compaction-related deformation (Rutter 1983, Houseknecht 1988, Onasch 1993). Diagenetic bedding-normal compaction should produce oblate strain ellipsoids with X- and Y-axes parallel to bedding and Z-axes clustered around the bedding normal (Couzens *et al.* 1993). However, the PSS data from the Tuscarora Sandstone of the Barclay anticline do not simply record such compaction-dominated deformation.

There are two possible explanations for this lack of pressure solution evidence for compaction. The first explanation considers the pre-existing grain fabric in the sandstone. Onasch (1993) showed that real grain populations deformed by pressure solution overestimate shortening magnitudes. Yet, examination of Figures 6a, 8a, and 8c in Onasch (1993) reveals a second source of overestimation for real grain fabrics parallel to the long axis of the strain ellipse. For compaction, elongation should be zero when measured parallel to bedding in a bed-normal measurement plane. Yet, pre-existing grain fabric creates an apparent volume loss of 5 to 15% and produces near-circular ellipses for 0 to 20% shortening. As a result, the near-spherical ellipsoids measured in the Barclay anticline may be an artifact of this second source of overestimation from measuring elongation for a simple uniaxial compaction.

A second possible explanation for near-spherical, rather than oblate, ellipsoids from the PSS data is that compactional shortening magnitudes may approximately equal layer-parallel shortening (LPS) magnitudes. If this is the case, apparent shortening effects of these two events parallel to strike (Onasch 1993) would need to have a magnitude equivalent to the real shortenings. Such a correspondence requires strong coincidence, particularly since apparent shortening exceeds real shortening for small strains (Onasch 1993). Thus, the first explanation for the strain geometry is more likely, because it is consistent with the observed grain fabrics and strain magnitudes. Thus, although the calculated strain ratios are small, there is a measurable amount of tectonic strain in the samples. An important implication of this interpretation is that grain-to-grain solution preceded tectonic deformation.

FINITE STRAIN ANALYSIS

Methodology

For each of the three mutually perpendicular thin sections from all 41 samples, boundaries of 200 quartz grains were digitized to determine finite strain with the normalized Fry method (Fry 1979, Erslev 1988). Original detrital quartz grain boundaries were identified from optically continuous cement overgrowths in cathodoluminescence photomicrographs, as recommended by Houseknecht (1988). Detrital grains preserve their original grain centers, permitting the use of quartz grains as strain markers in the Tuscarora Sandstone (Dunne *et al.* 1990). Strain ellipsoids were then calculated from the three mutually perpendicular strain ellipses derived for each sample (Appendix E) (Owens 1984). Sample sites were chosen to eliminate transgranular heterogeneous structures, such as microveins and stylolites, so as to measure homogeneous strain at the scale of 200-grain domains. Possible contributors to pervasive deformation at this scale are dislocation-related structures, fluid-inclusion planes, and pressure solution at the grain scale (Figures 10, 11). Such dislocation-related microstructures as undulatory extinction, deformation bands, and deformation lamellae are uniformly abundant throughout the Barclay anticline (Tables C.1, C.2;Figure 10a,b) and could be a potentially large source of finite strain. Pressure solution, in the form of grain-to-grain interpenetrations (Figure 12), is common throughout the Tuscarora Sandstone and is also possibly a major contributor to finite strain. Fluid inclusion planes (Figure 10a), however, are scarce, so their contribution to finite strain is small.

Strain magnitudes

Flinn plots for strain ratios (Figure 15a-e) reveal no apparent relationship between structural domain and strain magnitude. Strain ratios are small for all domains (Figure 15; Tables E.1, E.2) with ratios of less than 1.25. This result is consistent with measurements in previous studies of finite strain in quartz arenites of the central Appalachians (Couzens *et al.* 1993, Dunne & Caldanaro *in review*).

These small values may result from the cancelling effect of the two deformations that are thought to be prevalent in sandstones of the Central Appalachians: sedimentary compaction and layer-parallel shortening (Geiser 1974, Engelder 1979a, Engelder 1979b, Nickelsen 1979, Ferrill & Dunne 1989, Couzens *et al.* 1993, Dunne & Caldanaro *in review*). Pretectonic diagenetic compaction produces a bedding-normal flattening strain (Figure 15f), with R_{yz} much larger than the R_{xy} of about 1.00 (Ramsay & Wood 1973). Such compaction causes 10-30% shortening, with resulting strain ratios of 1.11-1.43. Regional LPS shortens normal to the compaction as approximately a plane strain or an axial-symmetric flattening. This deformation would reduce R_{yz} ratios while increasing R_{xy} (Couzens *et al.* 1993), which would keep strain ratios small, resulting in a pattern of data points for progressive deformation like that in Figure 15(f). If diagenetic compaction followed by LPS is the dominant source of finite strain in the Tuscarora Sandstone, the Flinn plots should resemble Figure 15(f). Although the measured strain ratios fall within the aforementioned range of values and some plots have data points distributed along a line of negative slope, the Flinn plots for the hanging wall domains do not compare simply to the ideal deformation sequence. This deviation from ideal in the plots may reflect additional deformations at the scale of 200-grain domains, or may result

Figure 15. Flinn plots of finite strain data. Data are divided into structural domains (a-e) and labels for data points correspond to sample numbers. Figure 15(f) illustrates the effect on finite strain values of layer-parallel shortening (LPS) overprinting pretectonic diagenetic compaction.

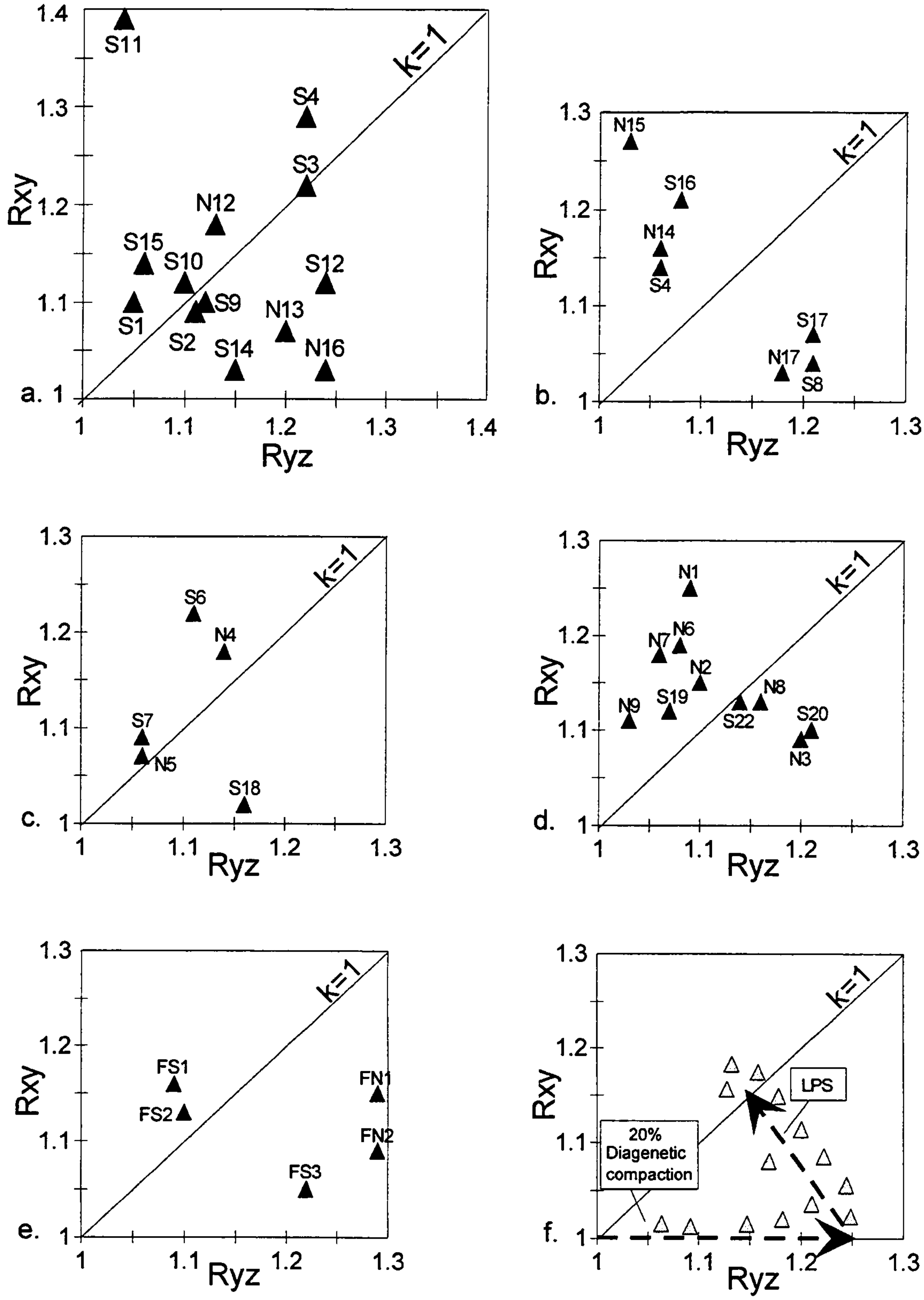

a.
Rxy
Ryz
k=1
S11
S4
S3
N12
S15
S10
S12
S9
S1
S2
N13
S14
N16
b.
N15
S16
N14
S4
S17
N17
S8
c.
S6
N4
S7
N5
S18
d.
N1
N7
N6
N2
N9
S19
S22
N8
S20
N3
e.
FS1
FS2
FN1
FN2
FS3
f.
LPS
20%
Diagenetic
compaction

from deforming grains that already possess a pre-compaction fabric.

Orientation data

Finite-strain ellipsoid axis orientations are depicted for both present-day bedding orientations and also for bedding rotated to the horizontal (Figure 16). Rotated bedding better reveals whether deformation, as represented by finite strain data, was geometrically related to layering or the present-day horizontal. If deformation at the scale of the 200-grain domains is dominated by layer-normal compaction and LPS, axes for strain ellipsoids would have more clearly defined polar and girdle distributions for the rotated data (Couzens *et al.* 1993). Rotated data do show clearer distributions than present-day data, which are interpreted as showing the relative importance of compaction and LPS to finite strain.

Most of the X- and Y-axes of the strain ellipsoids for the four hanging wall domains show bedding girdles, and all hanging wall Z-axes cluster around the bedding normal (Figure 16). These orientations are consistent with those predicted for deformation dominated by layer-normal shortening, such as pretectonic diagenetic compaction (Couzens *et al.* 1993). Because these orientations appear in most of the hanging wall domains, except for the backlimb region above the footwall ramp, it is interpreted that diagenetic compaction was a significant contributor to finite strain at the scale of the measured domains for the Tuscarora Sandstone in the field area and it had a greater magnitude than any tectonic contribution to finite strain.

Figure 16. Equal-area lower hemisphere projections depicting finite strain ellipsoid axial orientations. Data points are provided for the original bedding orientations ("(u)") and for bedding restored to horizontal ("(r)"), and is further divided into structural domains. Forelimb and backlimb ramp data were contoured using the Kamb (1959) method with 3σ contour interval.

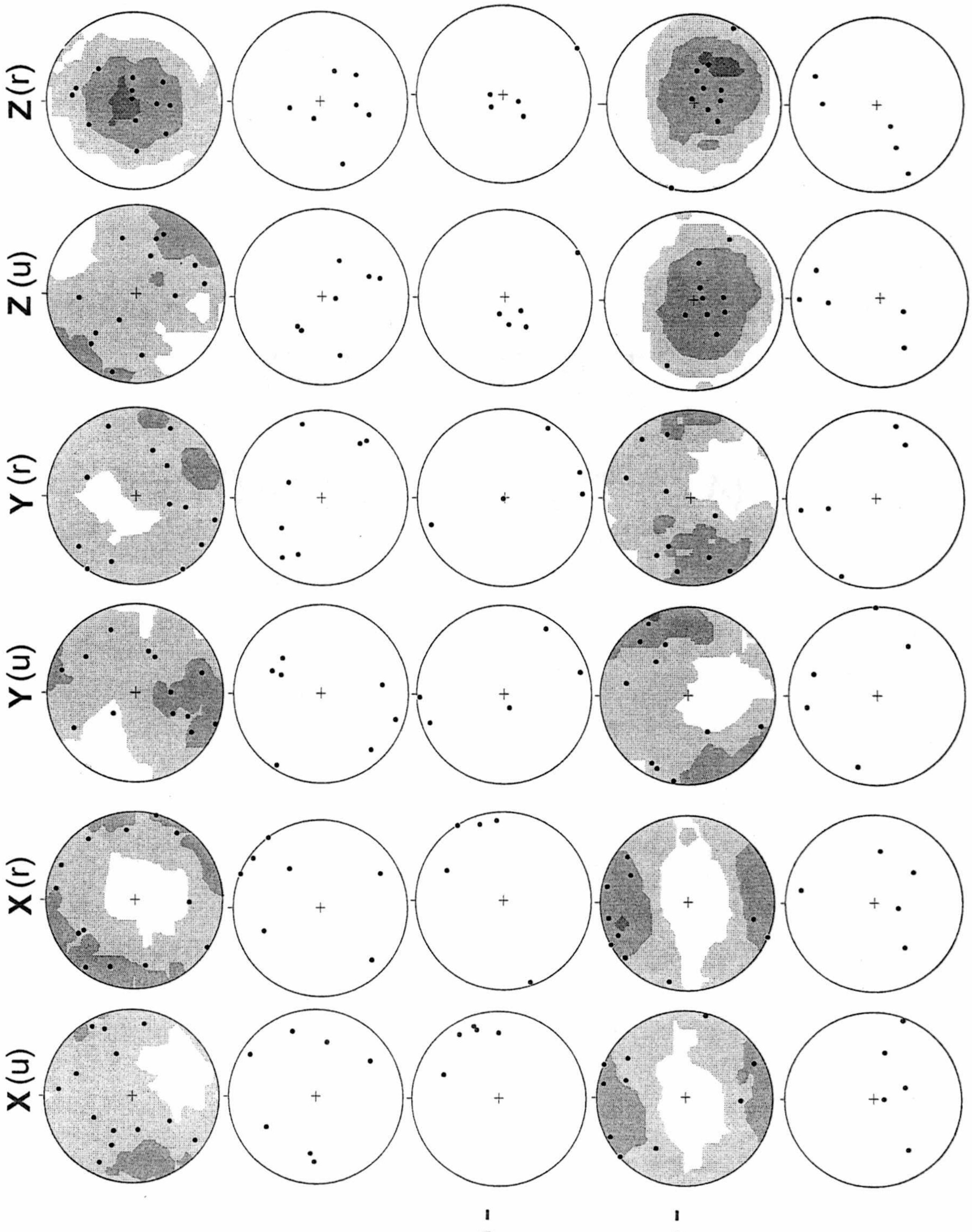
X (u)
X (r)
Y (u)
Y (r)
Z (u)
Z (r)
Forelimb (N=13)
Hinge (N=7)
Backlimb - Flat (N=5)
Backlimb - Ramp (N=10)
Footwall (N=5)

Comparison of PSS and finite strain

The pressure solution and finite strain data differ significantly. The finite-strain ellipsoid Z-axes have a distinct bedding-normal orientation, whereas the PSS Z-axes exhibit no preferred orientation. This result is unexpected because PSS records grain-to-grain solution of a mostly compactional origin, whereas finite strain records the effects of both compaction and the contribution of dislocation-related mechanisms during tectonic deformation. Therefore, the finite strain should have its compactional signal obscured by tectonic strain. The author interprets that the difference between the PSS and finite strain ellipsoid axial orientations results from finite strain recording both physical and chemical compaction, whereas the PSS method measures only the chemically driven grain-to-grain solution. The mechanical compaction is an additional 10-20% uniaxial volume loss (Onasch 1994), which doubles the solution-related shortening from PSS, and should produce a more pronounced compactional effect in the shape of the finite strain ellipsoid as compared to PSS ellipsoids.

Another difference between the two data sets is that the finite strain ellipsoids are less spherical than the PSS ellipsoids, indicated by the finite strain ratios that average 1.14 instead of 1.03. The less spherical shapes may result from two sources: the greater recorded compaction in the finite strain and the dislocation-related deformation. As mentioned previously, the finite strain records a greater compaction strain because it includes mechanical effects, but excludes the overestimation by the PSS method. Thus, finite-strain R_{yz} would be greater. Dislocation-related microstructures are abundant in the Tuscarora Sandstone and represent a pervasive tectonic deformation, probably LPS. Such deformation would increase the R_{xy} ratio for a pre-existing compactionally generated strain ellipsoid.

DISCUSSION

Comparison of the Barclay anticline to models for fault-related folds

The observed pattern of deformation in the Barclay anticline may be compared to the models for fault-related folds (Figures 1 and 5) to determine the cause of folding prior to, or during, transport over a footwall ramp. Fault-propagation folding with preservation of layer thickness is not a viable geometric choice (Figure 5a), because it requires an additional fold hinge and an overturned forelimb. The remaining three models can form the necessary geometry, yet they differ in their kinematic imprint at the micro- or mesoscale in the forelimb and main hinge.

The Barclay anticline does not contain deformation distributions at the microscale that correlate to fold domains. Patterns of microstructural deformation do not match the predicted pervasive deformations of the fold models. Instead, the anticline contains ubiquitous dislocation-related structures and grain-to-grain solution that resulted from diagenetic compaction and layer-parallel shortening, predating fold-thrust development. As a result, folding was accommodated through development of mesostructures and discontinuous microstructures, but not by pervasive, continuous microscale deformation.

The fault-bend fold and folding-after-fault-propagation models (Figures 5b and 5c) require considerable material transport through the main hinge to accommodate the change in hanging wall cutoff angle during fault displacement (Figure 6). Although bedding-parallel slip surfaces are abundant in the forelimb, at a spacing of one every 2 m, they terminate in the hinge and are absent in the backlimb. This geometry precludes material transport through the hinge by layer-parallel slip. Thus, the fault-bend fold and folding-after-fault-propagation models fail as explanations for the Barclay anticline.

The distribution of slip surfaces is consistent with flexural slip during break thrusting, because slip would be expected only in the limbs and not in the hinge. The absence of slip surfaces in the backlimb may indicate that the anticline developed as a kink fold with one active limb (Stewart & Alvarez 1991). Alternatively, it may mean that small magnitudes of slip for the gently dipping southeastern limb would be absorbed at unit boundaries or within the two weak "racetrack" layers. The appearance of more frequent bedding-parallel slip surfaces in locations with greater predicted flexural slip is consistent with observations from other folded quartz arenites in the Appalachians (Dunne 1986, Couzens & Dunne 1994, Dunne & Caldanaro *in review*). Folding by flexural slip would also explain the paucity of evidence for tangential longitudinal strain in the main hinge. The only evidence for such strain is the contraction faulting in the inner arcs of both profiles. The faults in the basal conglomerate of the south profile record small deformations and are interpreted to indicate a migrating hinge. The greater deformation in the north profile is consistent with hinge pinning during fold amplification. Hence, the Barclay anticline is best explained as a break-thrust fold which formed by flexural slip, with a migrating hinge that only pinned in the north profile where a secondary imbricate thrust developed.

The deformation history of the Barclay anticline consists first of folding through flexural slip, with fold amplification occurring through hinge migration. The fold was then faulted by the Barclay thrust, passing through one footwall bend in the process. Later minor folding in the footwall folded the Barclay thrust (Figure 3). The footwall syncline required by the break-thrust fold model may or may not be present; in the field, the footwall is covered where the syncline should be present.

The Barclay anticline and the concept of self-similarity

The two profiles of the Barclay anticline are similar in that they have the same microstructural abundances and similar strain magnitudes and orientations. They share a common fold shape, consisting of straight limbs, narrow hinge, steep forelimb, and gently dipping backlimb. The profiles cannot be interpreted as self-similar, however, because the imbricate fault is present only in the north profile and the thickness of the Juniata Formation above the Barclay thrust is greater in the south profile than in the north. As a result, the north profile does not represent an earlier stage of development for the south profile, which is a requirement for self-similar behavior as defined by Suppe and Medwedeff (1990) and Fischer and Woodward (1992). This result is also consistent with fold kinematics because break-thrust folding does not require self-similar development (Fischer *et al.* 1992).

CONCLUSIONS

(1) Break-thrust folding best explains the initiation of the Barclay anticline. The fold is interpreted to have formed by flexural slip, with a small amount of inner-arc contraction. Fold amplification occurred through hinge migration, perhaps due to kinking with only one rotating limb. After thrust propagation, the anticline was translated through one footwall fault bend to its present position. An important aspect of this result is that break-thrust folding may occur with hinge migration, in contrast to previous discussion (Fischer & Woodward 1992, Fischer *et al.* 1992). In this case, the characteristic that distinguishes break thrusting from other models with hinge migration is whether material transport occurred through the anticlinal hinge.

(2) Although the Barclay anticline displays many similar characteristics in the two profiles, it is not self-similar. The presence of an imbricate thrust in the north hinge and the different thicknesses of detached Juniata Formation between the two fold profiles preclude the possibility that the north profile represents an earlier stage of development of the south profile.

(3) This study again shows that geometry is an insufficient discriminator when determining the origin of a fault-related anticline. In the case of the Barclay anticline, geometric characteristics could eliminate only one likely possibility. Kinematic analysis is more discriminating, although detecting the difference between fault-bend folding and folding-after-fault-propagation may be difficult when the latter lacks a strong imprint from transport over footwall fault bends. Also, finite states of the deformation can discriminate between possible origins if

the contribution of both micro- and mesoscale structures are included. While incremental states are preferred for analysis, they are often not necessary.

(4) The Tuscarora Sandstone of the Barclay anticline folded in a manner characteristic of sandstone deformation in the central Appalachians: diagenesis by physical compaction and grain-to-grain solution; early pervasive, but not intense, tectonic dislocation-related deformation; and then discontinuous deformation by slip or dilation on bedding, faults, and veins.

REFERENCES

REFERENCES

Armstrong, P. A. & Bartley, J. M. 1993. Displacement and deformation associated with a lateral thrust termination, southern Golden Gate Range, southern Nevada, U. S. A. *J. Struct. Geol.* **15**, 721-735.

Bambach, R. K. 1987. The Ordovician-Silurian unconformity in western Virginia and adjacent West Virginia. *Appalachian Basin Industrial Associates*. **13**, 2-14.

Cardwell, D. H., Erwin, R. B. & Woodward, H. P. 1968. Geologic map of West Virginia. *W. Virginia Geol. & Econ. Surv. Map* 1, 1:250,000, 2 sheets.

Cecil, C. B. 1972. General geology of the Browns Mountain anticline, southeastern West Virginia. In: *Appalachian Structures: Origin, Evolution, and Possible Potential for New Exploration Frontiers* (edited by Lessing, P., Hayhurst, R. I., Barlow, J. A. & Woodfork, L. D.). West Virginia University and West Virginia Geological and Economical Survey. 181-193.

Chen, P. 1981. Lower Paleozoic stratigraphy, tectonics, paleogeography, and oil/gas possibilities in the central appalachians (West Virginia and adjacent states) -- Part 2. Measured sections. *W. Virginia Geol. & Econ. Surv. Rep. Invest.* **26-2**.

Colton, G. W. 1970. The Appalachian basin--Its depositional sequences and their geologic relationships. In: *Studies of Appalachian Geology: Central and Southern* (edited by Fisher, G. W., Pettijohn, F. J., Read, J. C., Jr. & Weaver, K. N.). Wiley-Interscience, New York, 5-47.

Couzens, B. A., Dunne, W. M., Onasch, C. M. & Glass, R. 1993. Strain variations and three-dimensional strain factorization at the transition from the southern to the central Appalachians. *J. Struct. Geol.* **15**, 451-464.

Couzens, B. A. & Dunne, W. M. 1994. Displacement transfer at thrust terminations: the Saltville thrust and Sinking Creek anticline, Virginia, U.S.A. *J. Struct. Geol.* **16**, 781-793.

Dean, S. L., Kulander, B. R. & Skinner, J. M. 1988. Structural chronology of the Alleghanian orogeny in southeastern West Virginia. *Bull. geol. Soc. Am.* **100**, 299-310.

Dorsch, J. 1993. Tectonics and sedimentation of the Taconic molasse in southwestern Virginia. Unpublished Ph.D. dissertation, University of Tennessee.

Dorsch, J., Bambach, R. K. & Driese, S. G. 1994. Basin-rebound origin for the "Tuscarora Unconformity" in southwestern Virginia and its bearing on the nature of the Taconic orogeny. *Am. J. Sci.* **294**, 237-255.

Dunne, W. M. 1986. Mesostructural development in detached folds: an example from West Virginia. *J. Geol.* **94**, 473-488.

Dunne, W. M., Onasch, C. M. & Williams, R. 1990. The problem of strain-marker centers and the Fry method. *J. Struct. Geol.* **12**, 933-938.

Dunne, W. M. & Caldanaro, A. J. *in review* Progressive deformation of a quartz arenite from diagenesis through folding and the roles of inhomogeneities.

Engelder, T. 1979a. Mechanisms for strain within the Upper Devonian clastic sequence of the Appalachian plateau, western New York. *Am. J. Sci.* **279**, 527-542.

Engelder, T. 1979b. The nature of deformation within the outer limits of the central Appalachian foreland fold and thrust belt in New York State. *Tectonophysics* **55**, 289-310.

Erslev, E. A. 1988. Normalized center-to-center strain analysis of packed aggregates. *J. Struct. Geol.* **10**, 201-209.

Faill, R. T. 1973. Kink-band folding, Valley and Ridge province, Pennsylvania. *Bull. geol. Soc. Am.* **84**, pp. 1289-1314.

Ferrill, D. A. & Dunne, W. M. 1989. Cover deformation above a blind duplex: an example from West Virginia, U.S.A. *J. Struct. Geol.* **11**, 421-431.

Fischer, M. P. & Woodward, N. B. 1992. The geometric analysis of foreland thrust systems. In: *Thrust Tectonics* (edited by McClay, K. L.). Chapman & Hall, London, 181-189.

Fischer, M. P., Woodward, N. B. & Mitchell, M. M. 1992. The kinematics of break-thrust folds. *J. Struct. Geol.* **14**, 451-460.

Fisher, D. M. & Anastasio, D. J. 1994. Kinematic analysis of a large-scale leading edge fold, Lost River Range, Idaho. *J. Struct. Geol.* **16**, 337-354.

Fry, N. 1979. Random point distributions and strain measurement in rocks. *Tectonophysics* **60**, 89-105.

Geiser, P. A. 1974. Cleavage in some sedimentary rocks of the central Valley and Ridge Province, Maryland. *Bull. geol. Soc. Am.* **85**, 1399-1412.

Gray, D. R. 1981. Cleavage-fold relationships and their implications for transected folds: an example from central Virginia. *J. Struct. Geol.* **3**, 265-277.

Groshong, R. H. Jr. 1988. Low temperature deformation mechanisms and their interpretation. *Bull. geol. Soc. Am.* **100**, 1329-1360.

Harris, A. G. 1979. Conodont color alteration, an organo-mineral metamorphic index, and its applications to Appalachian Basin geology. In: *Aspects of Diagenesis* (edited by Scholle, P. S. & Schulgar, P. R.). *Spec. Publ. Soc. econ. Paleont. Miner.* **26**, 3-16.

Hayes, A. W. 1974. Origin of the Tuscarora Formation (Lower Silurian), southwestern Virginia. Unpublished PhD. dissertation, Virginia Polytechnic Institute and State University.

Houseknecht, D. W. 1988. Intergranular pressure solution in four quartzose sandstones. *J. Sedim. Petrol.* **58**, 228-246.

Kamb, W. B. 1959. Ice petrofabric observations from Blue Glacier, Washington, in relation to theory and experiment. *J. geophys. Res.* **64**, 1891-1909.

Kulander, B. R. 1968. A structural analysis of Browns Mountain anticline in West Virginia. Unpublished Ph.D. dissertation, West Virginia University.

Kulander, B. R., Dean, S. L. & Lessing, P. 1986. The Browns Mountain anticlinorium, West Virginia. Geological Society of America Centennial Field Guide -- Southeastern Section, 101-104.

Lloyd, G. E. & Knipe, R. J. 1992. Deformation mechanism accommodating faulting of quartzite under upper crustal conditions. *J. Struct. Geol.* **14**, 127-143.

Mandelbrot, B. B. 1983. *The Fractal Geometry of Nature*. Freeman, New York.

McConnell, D. A. 1994. Fixed-hinge, basement-involved fault-propagation folds, Wyoming. *Bull. Am. Ass. Petrol. Geol.* **106**, 1583-1593.

Mitchell, M. M. & Woodward, N. B. 1988. Kink detachment fold in the southwest Montana fold and thrust belt. *Geology* **16**, 162-165.

Mitra, S. 1990. Fault-propagation folds: geometry, kinematic evolution, and hydorcarbon traps. *Bull. Am. Ass. Petrol. Geol.* **74**, 921-945.

Morley, C. K. 1994. Fold-generated imbricates: examples from the Caledonides of Southern Norway. *J. Struct. Geol.* **16**, 619-631.

Nickelsen, R. P. 1979. Sequence of structural stages of the Alleghany orogeny, at the Bear Valley strip mine, Shamokin, Pennsylvania. *Am. J. Sci.* **279**, 225-271.

Onasch, C. M. 1990. Microfractures and their role in deformation of a quartz arenite from the central Appalachian foreland. *J. Struct. Geol.* **12**, 883-894.

Onasch, C. M. 1993. Determination of pressure solution shortening in sandstones. *Tectonophysics* **227**, 145-159.

Onasch, C. M. 1994. Assessing brittle volume-gain and pressure solution volume-loss processes in quartz arenite. *J. Struct. Geol.* **16**, 519-530.

Onasch, C. M. & Dunne, W. M. 1993. Variation in quartz arenite deformation mechanisms between a roof sequence and duplexes. *J. Struct. Geol.* **15**, 465-475.

Owens, W. H. 1984. The calculation of a best-fit ellipsoid from elliptical sections on arbitrarily oriented planes. *J. Struct. Geol.* **6**, 571-577.

Pettijohn, F. J., Potter, P. E. & Siever, R. 1987. *Sand and Sandstone.* Springer-Verlag, New York.

Ramsay, J. G. 1967. *Folding and Fracturing of Rock.* McGraw-Hill, New York, 568 pp.

Ramsay, J. G. & Huber, M. I. 1983. *The Techniques of Modern Structural Geology, Volume 1: Strain Analysis.* Academic Press, Inc., Orlando.

Ramsay, J. G. & Huber, M. I. 1987. *The Techniques of Modern Structural Geology, Volume 2: Folds and Fractures.* Academic Press, Inc., Orlando.

Ramsay, J. G. & Wood, D. S. 1973. The geometric effects of volume change during deformation processes. *Tectonophysics* **16**, 263-277.

Ray, M. 1995. Personal communication.

Rich, R. L. 1934. Mechanics of low-angle overthrust faulting as illustrated by Cumberland thrust block, Virginia, Kentucky, and Tennessee. *Bull. Am. Ass. Petrol. Geol.* **18**, 1584-1596.

Rutter, E. H. 1983. Pressure solution in nature, theory, and experiment. *J. geol. Soc. Lond.* **140**, 725-740.

Sanderson, D. J. 1982. Models of strain variation in nappes and thrust sheets: A review. *Tectonophysics* **88**, 201-233.

Stewart, K. G. & Alvarez, W. 1991. Mobile-hinge kinking in layered rocks and models. *J. Struct. Geol.* **13**, 243-259.

Suppe, J. 1983. Geometry and kinematics of fault-bend folding. *Am. J. Sci.* **283**, 648-721.

Suppe, J. 1985. *Principles of Structural Geology.* Prentice-Hall, Englewood Cliffs, New Jersey.

Suppe, J. & Medwedeff, D. A. 1990. Geometry and kinematics of fault-propagation folding. *Eclog. geol. Helv.* **83**, 409-454.

Wilkerson, M. S., Medwedeff, D. A. & Marshak, S. 1991. Geometrical modeling of fault-related folds: a pseudo-three-dimensional approach. *J. Struct. Geol.* **13**, 801-812.

Williams, P. F. 1979. The development of asymmetrical folds in a cross-laminated siltstone. *J. Struct. Geol.* **1**, 19-30.

Willis, B. 1893. Mechanics of Appalachian structure. *U. S. Geological Survey Annual Report* 13 (1891-1892), part 2, 217-281.

Wiltschko, D. V. 1979. A mechanical model of thrust sheet deformation at a ramp. *J. geophys. Res.* **84**, 1091-1104.

Wiltschko, D. V., Medwedeff, D. A. & Millson, H. E. 1985. Distribution and mechanisms of strain within rocks on the northwest ramp of Pine Mountain block, southern Appalachian foreland: a field test of theory. *Bull. geol. Soc. Am.* **96**, 426-435.

Wu, S. 1993. Fractal strain distribution and its implications for cross-section balancing. *J. Struct. Geol.* **15**, 1497-1507.

APPENDICES

APPENDIX A: ORIENTATION DATA, SAMPLE PREPARATION, AND DATA COLLECTION

The first part of Appendix A contains a stratigraphic column of the Tuscarora Sandstone (Figure A.1) and bedding orientation data (Table A.2) collected at all the sample and station locales (Figure A.2), using the sample labels listed below (Table A.1). The second part of this appendix outlines and illustrates the procedures used in thin-section preparation and strain data collection.

Table A.1. Sample labeling key.

Sampling Label	Field Location
N	North profile
S	South profile
FN	Footwall of north profile
FS	Footwall of south profile

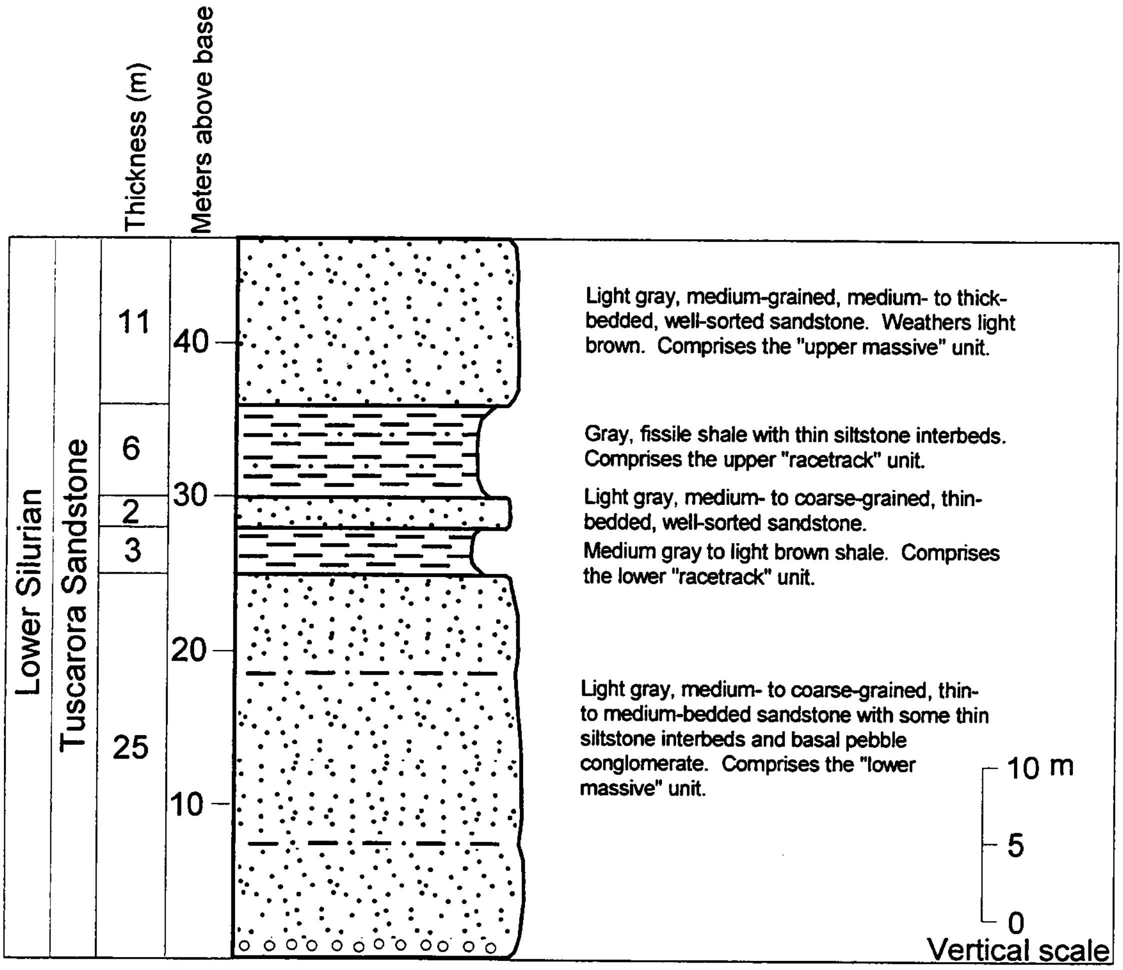

Figure A.1. Stratigraphic column of Silurian Tuscarora Sandstone (after Ray 1995).

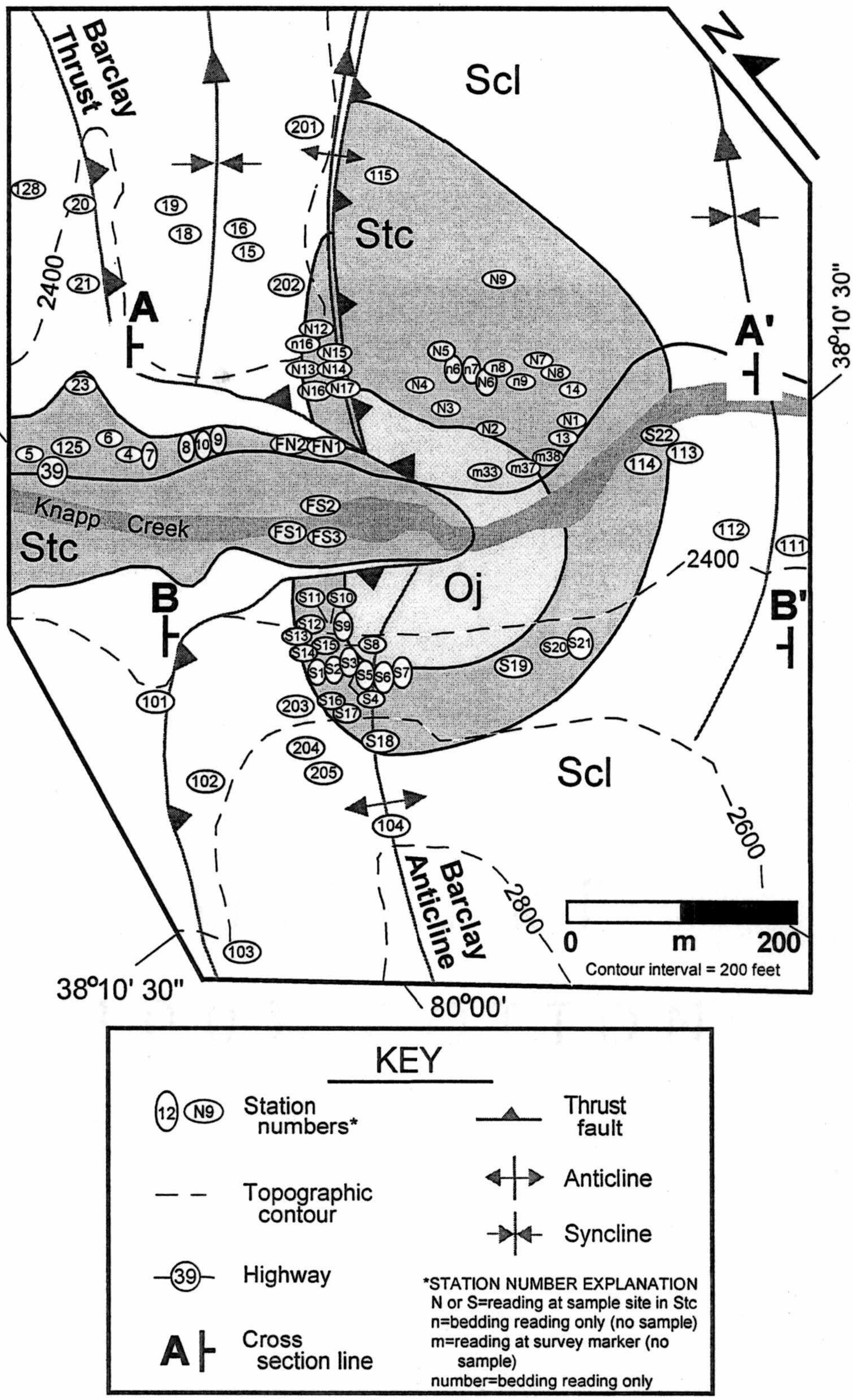

Figure A.2. Geologic map depicting sample and data stations. Location map and stratigraphic information are provided in Figure 2.

Table A.2. Bedding orientations of samples.

Field Location	Sample number	Strike/Dip	Quad.
	N1	014/20	SE
	N2	007/16	SE
	N3	345/17	SE
	N4	312/21	SE
	N5	341/17	SE
	N6	354/11	SE
	N7	013/12	SE
North	N8	002/12	SE
Profile	N9	351/11	SE
	N12	220/30	NW
	N13	027/84	NW
	N14	130/10	NW
	N15	071/14	NW
	N16	033/46	NW
	N17	038/77	NW
	FN1	315/07	FW
	FN2	327/08	FW
	S1	043/70	NW
	S2	039/51	NW
	S3	040/47	NW
	S4	054/34	NW
	S5	071/21	NW
	S6	173/07	SE
	S7	173/07	SE
	S8	026/11	NW
	S9	046/79	NW
	S10	030/46	NW
South	S11	038/73	NW
Profile	S12	035/75	NW
	S14	044/36	NW
	S15	052/12	NW
	S16	039/57	NW
	S17	043/34	NW
	S18	149/18	SE
	S19	017/26	SE
	S20	044/19	SE
	S22	030/13	SE
	FS1	033/23	FW
	FS2	022/19	FW
	FS3	054/13	FW

SAMPLE PREPARATION

Thin sections

Samples were cut into three mutually perpendicular billets from handspecimen blocks (Figure A.3). Orientations used for the thin sections are as follows:

b-section = bedding-parallel, looking down into bedding;

p-section = bedding- and dip-perpendicular, looking through the updip surface in the downdip direction;

v-section = bedding-perpendicular and dip-parallel, looking north.

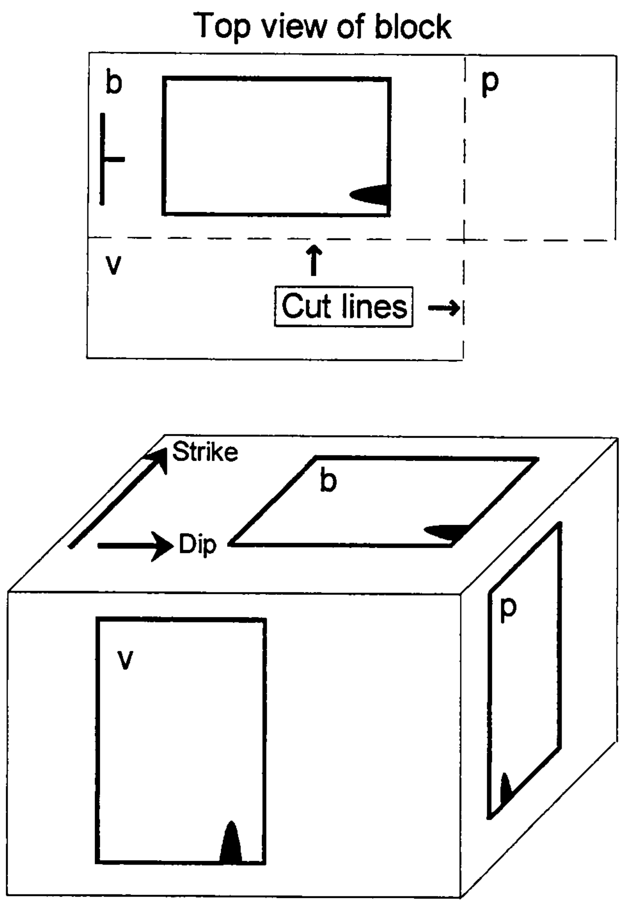

Figure A.3. Block of Tuscarora Sandstone.

Notching convention

A small notch was cut into each billet to record its relative orientation. Billets were notched and mounted to glass slides as illustrated in Figure A.4. All "b" and "p" sections were notched on the downdip and southerly end; all "v" sections were notched on the downdip end.

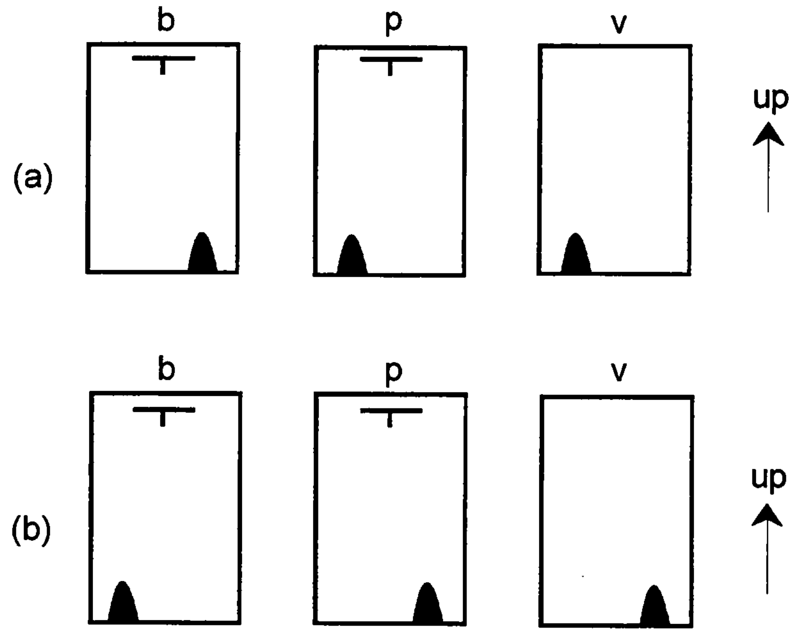

Figure A.4. Orientation of billets: (a) from NW-dipping samples; (b) from SE-dipping samples (rock side of slide facing up).

Thin section labels

An example of a thin section label is shown below in Figure A.5.

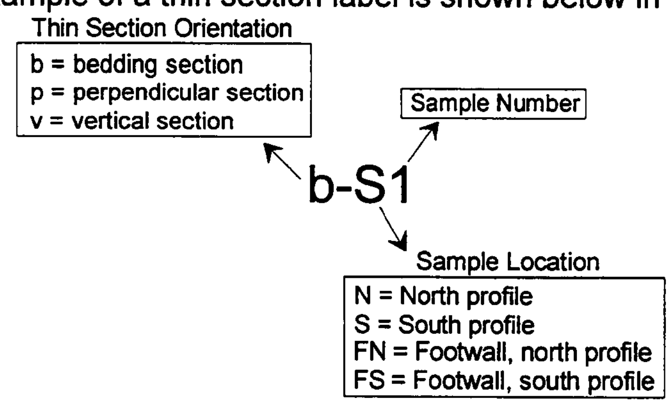

Figure A.5. Sample labeling convention.

DATA COLLECTION

Cathodoluminescence (CL) photomicroscopy

One to two photographs were taken for each thin section, and the field of view was large enough to ensure a 150-grain minimum for each photo. Ektachrome 400ASA film was used and exposure times averaged three to four minutes. For particularly dark sections, the film was exposed 1 stop down and push-processed 1 stop. All thin sections were arranged in the Citl Cold Cathode Luminescence Model MK3 vacuum chamber with their notches towards the front (Figure A.6). Photograph orientation corresponds to thin section orientation.

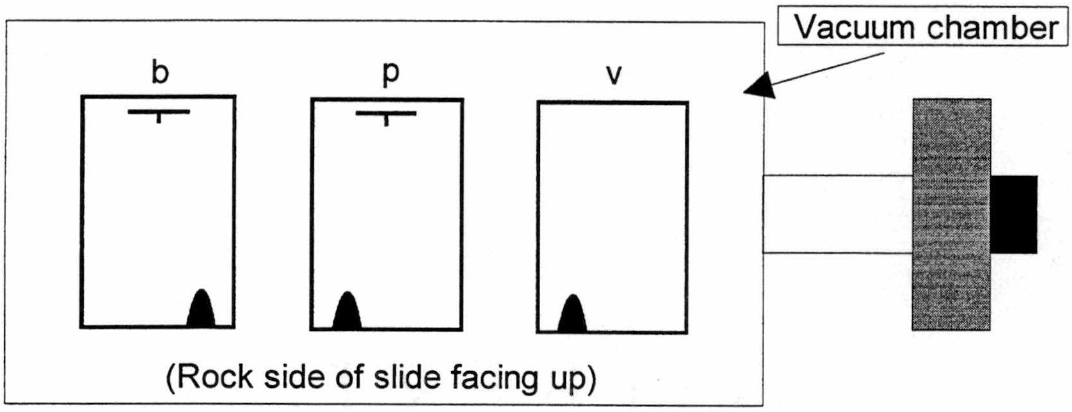

Figure A.6. Set-up for CL photomicroscopy.

Polarized light (PL) photomicroscopy

Polarized light photographs were taken of the same scenes photographed in CL. Sections were arranged the same as in CL.

Digitizing grain shapes

Only the CL images were digitized. Xerox color prints (8.5" x 11") were made for each slide photographed. The prints were arranged with the sample numbers at the top of the photo for strain analysis. Figure A.7 illustrates the arrangement of photos on the digitizing pad and the relationship of the photographs to the dip directions of the samples.

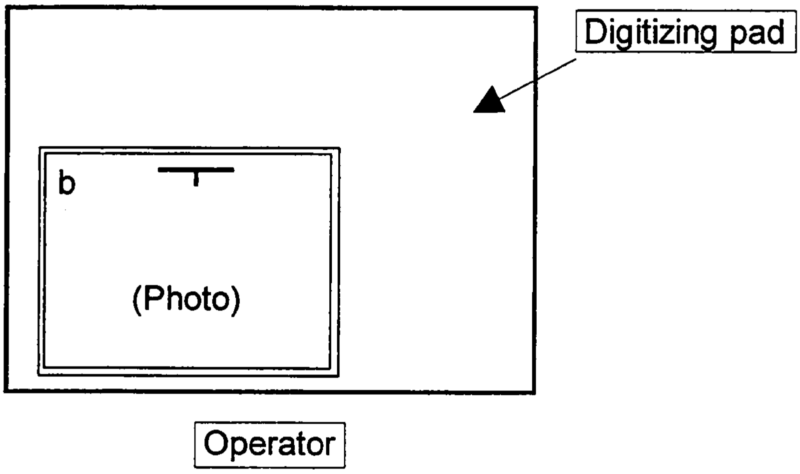

Figure A.7. Orientation of photographs on the digitizing pad.

APPENDIX B: MESOSTRUCTURAL OCCURRENCES

This appendix contains mesostructural occurrence data, including bedding orientations, for the northern and southern exposures of the Barclay anticline. Station locations are plotted on Figure A.2.

Table B.1. Mesostructural occurrences: north profile.

Station no.	Faults	Veins	Cataclastic zones	Solution surfaces	Bed-parallel slip	Orientation	Cross-bedding	Domain
N1	x	x	-	x	-	014, 20E	-	Backlimb-ramp
N2	x	x	-	-	-	007, 16E	x	Backlimb-ramp
n2	-	x	-	x	-	332, 17NE	-	Backlimb-ramp
N3	-	x	-	-	-	345, 17NE	-	Backlimb-ramp
N4	-	-	-	-	-	312, 21NE	-	Backlimb-flat
n5	-	-	-	x	-	339, 11NE	x	Backlimb-flat
N5	-	-	-	x	-	341, 17NE	-	Backlimb-flat
n6	-	-	-	x	-	341, 19E	x	Backlimb-flat
n7	-	-	-	x	-	348, 13E	x	Backlimb-ramp
N6	-	-	-	x	-	354, 11E	-	Backlimb-ramp
n8	-	-	-	x	-	354, 10E	-	Backlimb-ramp
n9	-	-	-	x	-	015, 18E	-	Backlimb-ramp
N7	-	-	-	x	-	013, 12E	-	Backlimb-ramp
N8	-	x	-	-	-	002, 12E	-	Backlimb-ramp
n12	-	-	-	-	-	018, 21E	-	Backlimb-ramp
N9	-	-	-	-	-	351, 11E	-	Backlimb-ramp
N12	-	-	-	x	-	220, 30W	-	Forelimb
N13	-	-	-	x	-	027, 84W	-	Forelimb
n16	-	-	-	x	-	230, 40W	-	Forelimb
N14	-	-	-	x	-	130, 10W	x	Hinge
N15	-	-	-	-	-	071, 14N	x	Hinge
N16	x	-	-	-	-	033, 46NW	-	Forelimb
N17	x	-	-	-	x	038, 77NW	-	Hinge
FN1	-	-	-	-	-	315, 7E	-	Footwall
FN2	-	-	-	-	-	327, 8E	-	Footwall

KEY: n=station; N=sample site; FN=footwall sample site; x=feature present; (-)=feature absent.

Table B.2. Mesostructural occurrences: south profile.

Station no.	Faults	Veins	Cataclastic zones	Solution surfaces	Bed-parallel slip	Orientation	Cross-bedding	Domain
S1	-	x	-	x	x	043, 70NW	x	Forelimb
S2	x	x	-	x	x	039, 51NW	x	Forelimb
S3	-	x	-	-	x	040, 47NW	-	Forelimb
S4	-	-	-	-	-	054, 34NW	-	Forelimb
S5	-	-	-	x	-	071, 21N	x	Hinge
S6	-	-	-	-	-	173, 7E	-	Backlimb-flat
S7	-	-	-	x	-	173, 7E	x	Backlimb-flat
S8	-	-	-	-	-	026, 11NW	-	Hinge
S9	x	-	x	-	x	046, 79NW	x	Forelimb
S10	x	-	x	-	x	030, 46NW	x	Forelimb
S11	x	-	x	-	x	038, 73NW	-	Forelimb
S12	x	x	-	-	x	035, 75NW	-	Forelimb
S13	x	-	-	-	x	042, 81NW	-	Forelimb
S14	-	-	-	-	-	044, 36NW	-	Forelimb
S15	-	-	-	-	-	052, 12NW	-	Forelimb
S16	x	-	-	x	x	039, 57NW	-	Hinge
S17	-	-	-	-	x	043, 34NW	x	Hinge
S18	-	-	-	x	-	149, 18NE	-	Backlimb-flat
S19	-	-	-	x	-	017, 26SE	-	Backlimb-ramp
S20	-	-	-	x	-	044, 19SE	-	Backlimb-ramp
S21	-	-	-	x	-	035, 7SE	-	Backlimb-ramp
S22	-	-	-	-	-	030, 13SE	-	Backlimb-ramp
FS1	-	-	-	-	-	033, 23NW	-	Footwall
FS2	-	-	-	-	-	022, 19NW	-	Footwall
FS3	-	-	-	-	-	054, 13NW	-	Footwall

KEY: S=station; X=sample site; FS=footwall sample site; x=feature present; (-)=feature absent.

APPENDIX C: MICROSTRUCTURAL DATA

This appendix contains microstructural data derived from point-counting 250 features in the "v" thin section of each sample. Data is divided into structural domains for both north and south profiles. Because many grains contained more than one type of microstructure, a total of 200 grains was used in calculating the percent occurrence for each feature.

Table C.1. Relative amounts of microstructures: north profile.

SAMPLE	Nothing	Undulatory Extinction	Subgrains	Deformation Lamellae	Deformation Bands	FIPs	Microveins	Cataclastic Bands	Stylolites	Sutured Grains	Total No. of Features
Forelimb											
v-N12	130	88	4	6	19	0	0	0	0	3	250
v-N13	140	88	3	3	13	0	3	0	0	0	250
v-N16	108	110	2	7	18	0	1	0	0	4	250
total:	378	286	9	16	50	0	4	0	0	7	
% of gr.:	0.630	0.477	0.015	0.027	0.083	0.000	0.007	0.000	0.000	0.012	
Hinge											
v-N14	157	71	6	5	10	0	1	0	0	0	250
v-N15	114	98	4	7	24	1	2	0	0	0	250
v-N17	101	89	6	3	20	11	11	9	0	0	250
total:	372	258	16	15	54	12	14	9	0	0	
% of gr.:	0.620	0.430	0.027	0.025	0.090	0.020	0.023	0.015	0.000	0.000	
Backlimb: flat											
v-N4	157	71	0	5	15	2	0	0	0	0	250
v-N5	83	78	3	33	23	25	5	0	0	0	250
total:	240	149	3	38	38	27	5	0	0	0	
% of gr.:	0.600	0.373	0.008	0.095	0.095	0.068	0.013	0.000	0.000	0.000	
Backlimb: ramp											
v-N1	137	67	1	26	15	1	3	0	0	0	250
v-N2	59	73	8	41	25	41	1	0	0	2	250
v-N3	131	70	2	13	14	18	2	0	0	0	250
v-N6	125	90	1	15	18	0	1	0	0	0	250
v-N7	124	67	6	19	29	3	2	0	0	0	250
v-N8	83	100	17	24	10	15	1	0	0	0	250
v-N9	86	98	15	17	22	10	1	0	0	1	250
total:	745	565	50	155	133	88	11	0	0	3	
% of gr.:	0.532	0.404	0.036	0.111	0.095	0.063	0.008	0.000	0.000	0.002	
Footwall											
v-FN1	152	76	0	5	14	2	1	0	0	0	250
v-FN2	161	63	3	6	13	0	3	0	0	1	250
total:	313	139	3	11	27	2	4	0	0	1	
% of gr.:	0.783	0.348	0.008	0.028	0.068	0.005	0.010	0.000	0.000	0.003	

Table C.2. Relative amounts of microstructures: south profile.

SAMPLE	Nothing	Undulatory Extinction	Subgrains	Deformation Lamellae	Deformation Bands	FIPs	Microveins	Cataclastic Bands	Stylolites	Sutured Grains	Total No. of Features
	Forelimb										
v-S1	94	108	2	11	14	18	3	0	0	0	250
v-S2	56	98	15	32	14	18	12	5	0	0	250
v-S3	77	103	20	1	9	18	10	11	0	1	250
v-S4	111	77	12	4	3	39	2	0	10	2	260
v-S9	143	78	5	3	3	14	2	1	0	1	250
v-S10	126	72	3	1	8	31	2	7	0	0	250
v-S11	140	62	6	11	7	22	1	1	0	0	250
v-S12	150	64	6	1	7	14	5	3	0	0	250
v-S14	68	98	13	32	16	19	2	2	0	0	250
v-S15	96	73	7	21	17	33	3	0	0	0	250
total:	1061	833	89	117	98	226	42	30	10	4	
% of gr.:	0.531	0.417	0.045	0.059	0.049	0.113	0.021	0.015	0.005	0.002	
	Hinge										
v-S5	59	91	13	16	18	52	1	0	0	0	250
v-S8	111	91	16	9	11	9	3	0	0	0	250
v-S16	44	78	18	34	15	44	7	10	0	0	250
v-S17	118	83	10	10	21	1	4	0	0	3	250
total:	332	343	57	69	65	106	15	10	0	3	
% of gr.:	0.415	0.429	0.071	0.086	0.081	0.133	0.019	0.013	0.000	0.004	
	Backlimb: flat										
v-S6	81	103	11	23	13	19	0	0	0	0	250
v-S7	116	79	12	3	9	27	4	0	0	0	250
v-S18	154	64	4	16	9	0	3	0	0	0	250
total:	351	246	27	42	31	46	7	0	0	0	
% of gr.:	0.585	0.410	0.045	0.070	0.052	0.077	0.012	0.000	0.000	0.000	
	Backlimb: ramp										
v-S19	100	98	3	21	22	5	1	0	0	0	250
v-S20	124	96	4	6	18	0	2	0	0	0	250
v-S22	138	76	0	17	16	0	3	0	0	0	250
total:	362	270	7	44	56	5	6	0	0	0	
% of gr.:	0.603	0.450	0.012	0.073	0.093	0.008	0.010	0.000	0.000	0.000	
	Footwall										
v-FS1	112	96	4	21	14	1	2	0	0	0	250
v-FS2	57	127	0	29	26	11	0	0	0	0	250
v-FS3	132	75	6	17	16	3	0	0	0	1	250
total:	301	298	10	67	56	15	2	0	0	1	
% of gr.:	0.502	0.497	0.017	0.112	0.093	0.025	0.003	0.000	0.000	0.002	

APPENDIX D: TWO- AND THREE-DIMENSIONAL ROTATED PSS INCREMENTAL STRAIN DATA

This appendix contains incremental strain data from grain to grain solution arranged by profile lines. All data are derived from application of the PSS method (Onasch 1993). Cathodoluminescent photomicrographs were used to define original grain shapes. These incremental strains were processed with bedding restored to the horizontal. Figure A.2 in Appendix A shows the sample locations. As with the finite strain data, the two-dimensional data are listed under the "Input Data" section. Each plane is represented by a letter: b (bed-parallel), p (bed-perpendicular, strike-parallel), and v (bed-perpendicular, dip-parallel). Three-dimensional data are listed under "Owens' Output Data" as axial stretch, axis trend, axis plunge, and X/Y and Y/Z axial ratios. The last column, entitled "Solution," refers to the solution generated by the Owens' method which is the most statistically sound (contains the least error) (Owens, 1984).

Table D.1. Two- and three-dimensional rotated PSS incremental strain data.

Owens' Method PSS Ellipsoid Calculations: Bedding Rotated to Horizontal

INPUT DATA							OWENS' OUTPUT DATA						
Sample	Orientation	Plane	Strike	Dip	Rake	Ratio	Axis	Stretch	Axis Trend	Axis Plunge	Rxy	Ryz	Solution
N1	014/00	b	14	0	136	1.08	z	0.96	54.6	22.1	1.05	1.04	Q33
		p	14	90	137	1.04	y	1.00	274.6	62.1			
		v	104	90	0	1.01	x	1.05	151.4	16.2			
N2	007/00	b	7	0	139	1.01	z	1.00	246.1	34.4	1.03	1.00	Q33
		p	7	90	19	1.04	y	1.00	120.2	40.6			
		v	97	90	90	1.02	x	1.03	359.9	30.6			
N3	345/00	b	345	0	90	1.02	z	0.98	345.0	0.0	1.02	1.02	Q33
		p	345	90	90	1.05	y	1.00	184.0	90.0			
		v	75	90	0	1.05	x	1.02	75.0	0.0			
N7	013/00	b	13	0	0	1.00	z	1.00	193.0	0.0	1.01	1.00	Q33
		p	13	90	90	1.02	y	1.00	103.0	0.0			
		v	103	90	90	1.01	x	1.01	288.8	90.0			
N9	351/00	b	351	0	0	1.00	z	0.98	261.0	60.5	1.01	1.03	Q33
		p	351	90	0	1.02	y	1.00	351.0	0.0			
		v	81	90	33	1.03	x	1.01	81.0	29.5			
N12	040/00	b	40	0	0	1.02	z	0.99	130.0	0.0	1.01	1.01	Q33
		p	40	90	0	1.02	y	1.00	330.3	90.0			
		v	310	90	90	1.02	x	1.01	220.0	0.0			
N13	027/00	b	27	0	0	1.02	z	0.99	297.0	0.0	1.01	1.01	Q33
		p	27	90	0	1.00	y	1.00	160.0	90.0			
		v	117	90	0	1.00	x	1.01	27.0	0.0			
N14	130/00	b	130	0	0	1.03	z	0.99	207.8	90.0	1.03	1.01	Q33
		p	130	90	0	1.03	y	1.00	40.0	0.0			
		v	40	90	0	1.01	x	1.03	310.0	0.0			
N16	033/00	b	33	0	0	1.01	z	0.98	160.8	90.0	1.01	1.02	Q33
		p	33	90	0	1.02	y	1.00	303.0	0.0			
		v	303	90	0	1.02	x	1.01	33.0	0.0			
FN1	315/00	b	315	0	0	1.10	z	0.96	45.0	0.0	1.04	1.04	Q33
		p	315	90	0	1.02	y	1.00	220.3	90.0			
		v	45	90	90	1.02	x	1.04	315.0	0.0			
S2	039/00	b	39	0	90	1.05	z	0.99	39.4	90.0	1.06	1.01	Q33
		p	39	90	0	1.00	y	1.00	219.0	0.0			
		v	309	90	0	1.07	x	1.06	309.0	0.0			
S5	071/00	b	71	0	90	1.01	z	0.99	350.4	90.0	1.00	1.01	Q33
		p	71	90	0	1.02	y	1.00	161.0	0.0			
		v	341	90	0	1.00	x	1.00	251.0	0.0			
S7	353/00	b	353	0	90	1.02	z	0.99	83.0	55.0	1.06	1.02	Q33
		p	353	90	90	1.02	y	1.00	173.0	0.0			
		v	83	90	153	1.08	x	1.06	263.0	35.0			
S9	046/00	b	46	0	128	1.06	z	0.98	114.3	90.0	1.06	1.02	Q33
		p	46	90	0	1.05	y	1.00	267.6	0.0			
		v	316	90	0	1.05	x	1.06	357.6	0.0			
S12	035/00	b	35	0	0	1.01	z	0.99	184.1	90.0	1.00	1.01	Q33
		p	35	90	0	1.01	y	1.00	305.0	0.0			
		v	305	90	0	1.02	x	1.00	35.0	0.0			
S14	044/00	b	44	0	0	1.02	z	0.99	71.0	90.0	1.01	1.01	Q33
		p	44	90	90	1.02	y	1.00	224.0	0.0			
		v	314	90	0	1.05	x	1.01	314.0	0.0			
S16	039/00	b	39	0	0	1.01	z	1.00	129.0	0.0	1.04	1.00	Q33
		p	39	90	41	1.04	y	1.00	219.0	36.7			
		v	309	90	90	1.04	x	1.04	39.0	53.3			
S19	017/00	b	17	0	0	1.00	z	0.99	17.0	65.9	1.00	1.01	Q33
		p	17	90	132	1.01	y	1.00	197.0	24.1			
		v	107	90	0	1.02	x	1.00	287.0	0.0			
S22	030/00	b	30	0	0	1.01	z	0.99	300.0	0.0	1.02	1.01	Q33
		p	30	90	0	1.03	y	1.00	147.6	90.0			
		v	300	90	90	1.02	x	1.02	30.0	0.0			
FS1	033/00	b	33	0	137	1.10	z	0.99	83.5	0.0	1.09	1.01	Q33
		p	33	90	0	1.05	y	1.00	258.3	90.0			
		v	303	90	0	1.02	x	1.09	353.5	0.0			

APPENDIX E: TWO- AND THREE-DIMENSIONAL ROTATED AND UNROTATED FINITE STRAIN DATA

This appendix contains processed finite strain data arranged by profile, using the sample labels listed in Table A.1. All data are from cathodoluminescent photomicrographs. Strain data with bedding rotated to horizontal are shown in the first half (Table E.1) and data with true field orientations are shown in the second half (Table E.2). A map depicting sample locations is included in Appendix A (Figure A.2). Two-dimensional data are listed under the "Input Data" section. Each plane is represented by a letter: b (bed-parallel), p (bed-perpendicular, strike-parallel), and v (bed-perpendicular, dip-parallel). Three-dimensional data are listed under "Owens' Output Data" as axial stretch, axis trend, axis plunge, and XY and Y/Z axial ratios. The last column, entitled "Solution," refers to the solution generated by the Owens' method which is the most statistically sound (contains the least error) (Owens, 1984).

Table E.1. Two- and three-dimensional rotated finite strain data.

Owens' Method Ellipsoid Calculations: Bedding Rotated to Horizontal

INPUT DATA							OWENS' OUTPUT DATA						
Sample	Orientation	Plane	Strike	Dip	Rake	Ratio	Axis	Stretch	Axis Trend	Axis Plunge	Rxy	Ryz	Solution
N1	014/00	b	14	0	148	1.26	z	0.92	66.6	84.6	1.25	1.09	Q33
		p	14	90	178	1.17	y	1.00	241.2	5.3			
		v	104	90	178	1.23	x	1.25	331.2	0.5			
N2	007/00	b	7	0	153	1.17	z	0.91	216.2	62.1	1.15	1.10	Q33
		p	7	90	28	1.18	y	1.00	70.3	23.7			
		v	97	90	2	1.13	x	1.15	334.1	13.9			
N3	345/00	b	345	0	98	1.22	z	0.84	173.1	65.1	1.09	1.20	Q33
		p	345	90	16	1.27	y	1.00	17.3	22.9			
		v	75	90	1	1.13	x	1.09	283.4	9.1			
N4	312/00	b	312	0	134	1.17	z	0.88	314.9	74.6	1.18	1.14	Q33
		p	312	90	164	1.22	y	1.00	177.1	11.5			
		v	42	90	4	1.23	x	1.18	85.1	10.1			
N5	341/00	b	341	0	92	1.05	z	0.95	1.9	79.3	1.07	1.06	Q33
		p	341	90	158	1.04	y	1.00	160.6	10.0			
		v	71	90	177	1.15	x	1.07	251.2	3.8			
N6	354/00	b	354	0	114	1.17	z	0.93	204.2	74.9	1.19	1.08	Q33
		p	354	90	6	1.28	y	1.00	49.9	13.7			
		v	84	90	179	1.03	x	1.19	318.3	6.3			
N7	013/00	b	13	0	35	1.11	z	0.94	117.5	4.5	1.18	1.06	Q33
		p	13	90	17	1.22	y	1.00	215.4	60.5			
		v	103	90	88	1.17	x	1.18	25.0	29.1			
N8	002/00	b	2	0	20	1.11	z	0.86	123.6	73.1	1.13	1.16	Q33
		p	2	90	7	1.33	y	1.00	279.6	15.5			
		v	92	90	162	1.14	x	1.13	11.4	6.5			
N9	351/00	b	351	0	48	1.11	z	0.98	153.7	61.0	1.11	1.03	Q33
		p	351	90	22	1.08	y	1.00	300.4	24.8			
		v	81	90	12	1.07	x	1.11	37.0	14.0			
N12	040/00	b	40	0	43	1.21	z	0.89	332.6	41.8	1.18	1.13	Q33
		p	40	90	4	1.13	y	1.00	192.7	40.5			
		v	310	90	133	1.20	x	1.18	83.1	21.4			
N13	027/00	b	27	0	4	1.07	z	0.83	145.8	57.0	1.07	1.20	Q33
		p	27	90	40	1.13	y	1.00	237.1	0.8			
		v	117	90	156	1.28	x	1.07	327.6	33.0			
N14	130/00	b	130	0	52	1.12	z	0.94	250.4	25.5			
		p	130	90	14	1.22	y	1.00	25.5	56.1	1.16	1.06	Q33
		v	40	90	88	1.12	x	1.16	150.0	20.8			
N15	071/00	b	71	0	171	1.16	z	0.97	194.5	41.9	1.27	1.03	Q33
		p	71	90	54	1.26	y	1.00	303.4	20.0			
		v	341	90	49	1.10	x	1.27	52.1	41.5			
N16	033/00	b	33	0	108	1.11	z	0.81	224.8	46.6	1.03	1.24	Q33
		p	33	90	51	1.23	y	1.00	21.2	40.9			
		v	303	90	172	1.21	x	1.03	121.8	12.0			
N17	038/00	b	38	0	79	1.08	z	0.85	185.5	55.5	1.03	1.18	Q33
		p	38	90	25	1.19	y	1.00	75.0	13.6			
		v	308	90	32	1.14	x	1.03	336.6	31.1			
FN1	315/00	b	315	0	4	1.21	z	0.78	244.8	44.9	1.15	1.29	Q33
		p	315	90	135	1.21	y	1.00	352.0	16.6			
		v	45	90	39	1.38	x	1.15	96.7	40.4			
FN2	327/00	b	327	0	113	1.24	z	0.77	1.0	37.8	1.09	1.29	Q33
		p	327	90	135	1.25	y	1.00	117.9	30.3			
		v	57	90	137	1.27	x	1.09	234.6	37.5			

Table E.1. (continued)

Owens' Method Ellipsoid Calculations: Bedding Rotated to Horizontal

INPUT DATA							OWENS' OUTPUT DATA						
Sample	Orientation	Plane	Strike	Dip	Rake	Ratio	Axis	Stretch	Axis Trend	Axis Plunge	Rxy	Ryz	Solution
S1	042/00	b	42	0	176	1.17	z	0.96	57.2	87.2	1.10	1.05	Q33
		p	42	90	165	1.08	y	1.00	303.4	1.1			
		v	312	90	0	1.09	x	1.10	213.4	2.6			
S2	039/00	b	39	0	99	1.13	z	0.90	43.2	44.3	1.09	1.11	Q33
		p	39	90	150	1.19	y	1.00	290.2	21.2			
		v	309	90	100	1.04	x	1.09	182.2	37.7			
S3	040/00	b	40	0	92	1.13	z	0.82	185.6	56.4	1.22	1.22	Q33
		p	40	90	36	1.24	y	1.00	68.3	17.0			
		v	310	90	23	1.42	x	1.22	328.9	28.1			
S4	054/00	b	54	0	50	1.50	z	0.82	13.2	33.1	1.29	1.22	Q33
		p	54	90	146	1.18	y	1.00	194.3	56.9			
		v	324	90	153	1.20	x	1.29	103.5	0.5			
S5	071/00	b	71	0	158	1.14	z	0.94	346.8	60.9	1.14	1.06	Q33
		p	71	90	165	1.15	y	1.00	126.0	22.9			
		v	341	90	152	1.10	x	1.14	223.5	17.0			
S6	353/00	b	353	0	42	1.12	z	0.90	226.1	62.1	1.22	1.11	Q33
		p	353	90	22	1.26	y	1.00	121.8	7.5			
		v	83	90	37	1.17	x	1.22	28.0	26.7			
S7	353/00	b	353	0	83	1.11	z	0.95	202.1	74.5	1.09	1.06	Q33
		p	353	90	11	1.07	y	1.00	339.8	11.6			
		v	83	90	12	1.13	x	1.09	71.9	10.1			
S8	026/00	b	26	0	179	1.13	z	0.83	115.4	58.7	1.04	1.21	Q33
		p	26	90	0	1.17	y	1.00	291.7	31.3			
		v	116	90	153	1.22	x	1.04	22.7	1.7			
S9	046/00	b	46	0	43	1.04	z	0.89	185.0	69.0	1.10	1.12	Q33
		p	46	90	12	1.26	y	1.00	318.4	14.8			
		v	316	90	31	1.07	x	1.10	52.3	14.6			
S10	030/00	b	30	0	95	1.15	z	0.91	81.4	80.4	1.12	1.10	Q33
		p	30	90	176	1.12	y	1.00	215.6	6.7			
		v	300	90	9	1.21	x	1.12	306.4	6.8			
S11	038/00	b	38	0	40	1.31	z	0.96	6.1	29.6	1.39	1.04	Q33
		p	38	90	138	1.22	y	1.00	136.2	48.6			
		v	308	90	29	1.15	x	1.39	260.0	26.1			
S12	035/00	b	35	0	89	1.16	z	0.81	88.5	68.1	1.12	1.24	Q33
		p	35	90	169	1.28	y	1.00	197.1	7.3			
		v	305	90	30	1.28	x	1.12	289.8	20.5			
S14	044/00	b	44	0	148	1.04	z	0.87	265.0	73.0	1.03	1.15	Q33
		p	44	90	12	1.18	y	1.00	116.9	14.5			
		v	314	90	169	1.14	x	1.03	24.7	8.6			
S15	052/00	b	52	0	150	1.16	z	0.95	266.3	42.7	1.14	1.06	Q33
		p	52	90	59	1.07	y	1.00	109.6	44.9			
		v	322	90	0	1.11	x	1.14	7.5	11.9			
S16	039/00	b	39	0	18	1.22	z	0.93	144.0	48.1	1.21	1.08	Q33
		p	39	90	3	1.27	y	1.00	322.5	41.9			
		v	309	90	51	1.07	x	1.21	53.1	0.7			
S17	043/00	b	43	0	176	1.17	z	0.83	288.9	72.5	1.07	1.21	Q33
		p	43	90	14	1.19	y	1.00	127.5	16.6			
		v	313	90	169	1.25	x	1.07	35.9	5.3			
S18	329/00	b	329	0	88	1.15	z	0.87	147.7	1.4	1.02	1.16	Q33
		p	329	90	89	1.19	y	1.00	318.0	88.6			
		v	59	90	0	1.06	x	1.02	57.7	0.2			

Table E.1. (continued)

Owens' Method Ellipsoid Calculations: Bedding Rotated to Horizontal

INPUT DATA							OWENS' OUTPUT DATA						
Sample	Orientation	Plane	Strike	Dip	Rake	Ratio	Axis	Stretch	Axis Trend	Axis Plunge	Rxy	Ryz	Solution
S19	017/00	b	17	0	6	1.14	z	0.93	111.0	50.9	1.12	1.07	Q33
		p	17	90	0	1.17	y	1.00	294.0	39.1			
		v	107	90	137	1.07	x	1.12	202.8	1.5			
S20	044/00	b	44	0	143	1.15	z	0.83	93.7	59.5	1.10	1.21	Q33
		p	44	90	157	1.17	y	1.00	252.3	28.7			
		v	314	90	18	1.29	x	1.10	347.5	9.3			
S22	030/00	b	30	0	145	1.17	z	0.88	284.0	0.5	1.13	1.14	Q33
		p	30	90	170	1.18	y	1.00	15.2	67.2			
		v	300	90	92	1.26	x	1.13	193.8	22.8			
FS1	033/00	b	33	0	114	1.18	z	0.91	244.6	13.8	1.16	1.09	Q33
		p	33	90	91	1.11	y	1.00	348.8	44.9			
		v	303	90	129	1.18	x	1.16	142.0	41.8			
FS2	022/00	b	22	0	92	1.15	z	0.91	25.0	22.5	1.13	1.10	Q33
		p	22	90	130	1.18	y	1.00	293.0	4.7			
		v	292	90	91	1.21	x	1.13	191.9	67.0			
FS3	054/00	b	54	0	94	1.20	z	0.82	234.9	65.7	1.05	1.22	Q33
		p	54	90	15	1.33	y	1.00	105.2	16.1			
		v	324	90	174	1.06	x	1.05	9.9	17.8			

Table E.2. Two- and three-dimensional unrotated finite strain data.

Owens' Method Ellipsoid Calculations: Bedding Unrotated

INPUT DATA							**OWENS' OUTPUT DATA**						
Sample	Orientation	Plane	Strike	Dip	Rake	Ratio	Axis	Stretch	Axis Trend	Axis Plunge	Rxy	Ryz	Solution
N1	014/20	b	14	20	148	1.26	z	0.92	298.7	74.9	1.25	1.09	Q33
		p	14	110	178	1.17	y	1.00	61.0	8.2			
		v	104	90	18	1.23	x	1.25	152.8	12.6			
N2	007/16	b	7	16	153	1.17	z	0.91	235.1	52.3	1.16	1.10	Q33
		p	7	106	28	1.18	y	1.00	65.7	37.2			
		v	97	90	18	1.13	x	1.16	331.8	5.1			
N3	345/17	b	345	17	98	1.22	z	0.84	200.0	59.6	1.10	1.19	Q33
		p	345	107	16	1.27	y	1.00	12.0	30.2			
		v	75	90	18	1.13	x	1.10	104.1	3.5			
N4	312/21	b	312	21	134	1.17	z	0.88	260.6	64.8	1.18	1.14	Q33
		p	312	111	164	1.22	y	1.00	358.2	3.6			
		v	42	90	25	1.23	x	1.18	89.8	24.9			
N5	341/17	b	341	17	92	1.05	z	0.95	289.4	73.7	1.07	1.06	Q33
		p	341	107	158	1.04	y	1.00	163.5	9.7			
		v	71	90	14	1.15	x	1.07	71.2	12.9			
N6	354/11	b	354	11	114	1.17	z	0.93	224.7	71.5	1.19	1.07	Q33
		p	354	101	6	1.28	y	1.00	47.9	18.5			
		v	84	90	10	1.03	x	1.19	317.6	1.0			
N7	013/12	b	13	12	35	1.11	z	0.94	120.0	20.8	1.18	1.06	Q33
		p	13	102	17	1.22	y	1.00	238.8	51.7			
		v	103	90	100	1.17	x	1.18	17.0	30.5			
N8	002/12	b	2	12	20	1.11	z	0.86	165.1	80.8	1.13	1.16	Q33
		p	2	102	7	1.33	y	1.00	279.3	3.8			
		v	92	90	174	1.14	x	1.13	9.8	8.4			
N9	351/11	b	351	11	48	1.11	z	0.98	174.2	62.4	1.11	1.03	Q33
		p	351	101	22	1.08	y	1.00	297.8	16.2			
		v	81	90	23	1.07	x	1.11	34.5	21.8			
N12	040/30	b	40	150	43	1.21	z	0.88	286.6	9.8	1.14	1.14	Q33
		p	40	60	4	1.13	y	1.00	181.2	57.1			
		v	310	90	103	1.20	x	1.14	22.6	31.1			
N13	027/84	b	27	96	4	1.07	z	0.85	312.0	24.5	1.10	1.17	Q33
		p	27	6	40	1.13	y	1.00	204.2	33.9			
		v	117	90	72	1.28	x	1.10	70.2	46.0			
N14	130/10	b	130	10	52	1.12	z	0.95	252.3	30.8	1.17	1.05	Q33
		p	130	100	14	1.22	y	1.00	25.0	48.7			
		v	220	90	98	1.12	x	1.17	146.4	24.7			
N15	071/14	b	71	166	171	1.16	z	0.97	300.9	52.5	1.27	1.03	Q33
		p	71	76	54	1.26	y	1.00	197.7	9.9			
		v	161	90	35	1.10	x	1.27	100.5	35.8			
N16	033/46	b	33	134	108	1.11	z	0.81	170.9	24.1	1.03	1.24	Q33
		p	33	44	51	1.23	y	1.00	68.4	25.8			
		v	123	90	126	1.21	x	1.03	297.9	53.3			
N17	038/77	b	38	103	79	1.08	z	0.85	161.8	29.6	1.03	1.18	Q33
		p	38	13	25	1.19	y	1.00	41.9	41.2			
		v	128	90	135	1.14	x	1.03	274.9	34.6			
FN1	315/07	b	315	7	4	1.21	z	0.78	242.9	38.4	1.15	1.28	Q33
		p	315	97	135	1.21	y	1.00	350.6	21.0			
		v	45	90	46	1.38	x	1.15	102.5	44.2			
FN2	327/08	b	327	8	113	1.24	z	0.77	355.4	41.9	1.09	1.29	Q33
		p	327	98	135	1.25	y	1.00	122.3	33.8			
		v	57	90	145	1.27	x	1.09	234.7	29.6			

Table E.2. (continued)

Owens' Method Ellipsoid Calculations: Bedding Unrotated

INPUT DATA							OWENS' OUTPUT DATA						
Sample	Orientation	Plane	Strike	Dip	Rake	Ratio	Axis	Stretch	Axis Trend	Axis Plunge	Rxy	Ryz	Solution
S1	042/54	b	42	138	176	1.17	z	0.92	316.3	36.8	1.08	1.09	Q33
		p	42	48	165	1.08	y	1.00	108.2	49.7			
		v	312	90	126	1.09	x	1.08	215.5	14.1			
S2	039/51	b	39	129	99	1.13	z	0.87	75.3	34.7	1.04	1.16	Q33
		p	39	39	150	1.19	y	1.00	329.0	22.1			
		v	309	90	49	1.04	x	1.04	213.2	47.0			
S3	040/47	b	40	140	92	1.13	z	0.81	181.7	53.8	1.18	1.24	Q33
		p	40	50	36	1.24	y	1.00	34.6	31.6			
		v	130	90	156	1.42	x	1.18	294.5	15.8			
S4	054/34	b	54	146	50	1.03	z	0.85	114.4	27.2	1.06	1.18	Q33
		p	54	56	146	1.18	y	1.00	16.2	15.4			
		v	144	90	119	1.20	x	1.06	260.0	58.1			
S5	071/21	b	71	159	158	1.14	z	0.94	157.3	39.9	1.14	1.06	Q33
		p	71	69	165	1.15	y	1.00	24.0	39.3			
		v	161	90	131	1.10	x	1.14	270.9	25.6			
S6	353/07	b	353	7	42	1.12	z	0.90	232.5	56.3	1.22	1.11	Q33
		p	353	97	22	1.26	y	1.00	122.5	12.8			
		v	83	90	44	1.17	x	1.22	24.8	30.6			
S7	353/07	b	353	7	83	1.11	z	0.95	219.4	70.2	1.09	1.06	Q33
		p	353	97	11	1.07	y	1.00	338.5	9.9			
		v	83	90	19	1.13	x	1.09	71.5	17.0			
S8	026/11	b	26	11	179	1.13	z	0.82	115.5	51.6	1.01	1.21	Q33
		p	26	79	0	1.17	y	1.00	226.8	16.0			
		v	116	90	142	1.22	x	1.01	327.9	33.8			
S9	046/79	b	46	101	43	1.04	z	0.90	154.0	26.8	1.11	1.11	Q33
		p	46	11	12	1.26	y	1.00	315.2	61.9			
		v	136	90	132	1.07	x	1.11	60.0	7.8			
S10	030/46	b	30	134	95	1.15	z	0.91	110.3	51.5	1.12	1.10	Q33
		p	30	44	176	1.12	y	1.00	201.3	0.8			
		v	120	90	143	1.21	x	1.12	291.9	38.5			
S11	038/73	b	38	107	40	1.31	z	0.80	264.0	31.5	1.11	1.25	Q33
		p	38	17	138	1.22	y	1.00	119.1	53.2			
		v	308	90	136	1.15	x	1.11	4.9	17.1			
S12	035/75	b	35	105	89	1.16	z	0.81	109.0	34.5	1.11	1.23	Q33
		p	35	15	169	1.28	y	1.00	214.7	21.5			
		v	125	90	135	1.28	x	1.11	330.2	47.6			
S14	044/36	b	44	144	148	1.04	z	0.93	302.5	62.2	1.11	1.08	Q33
		p	44	54	12	1.18	y	1.00	163.8	21.6			
		v	314	90	133	1.14	x	1.11	66.9	16.7			
S15	052/12	b	52	168	150	1.16	z	0.98	356.8	35.7	1.18	1.02	Q33
		p	52	78	59	1.07	y	1.00	209.9	49.3			
		v	322	90	168	1.11	x	1.18	99.3	16.8			
S16	039/57	b	39	123	18	1.22	z	0.93	185.4	77.2	1.21	1.07	Q33
		p	39	33	3	1.27	y	1.00	301.8	5.8			
		v	309	90	174	1.07	x	1.21	32.9	11.4			
S17	043/34	b	43	146	176	1.17	z	0.86	309.5	53.6	1.13	1.16	Q33
		p	43	56	14	1.19	y	1.00	171.8	28.7			
		v	313	90	135	1.25	x	1.13	69.9	20.5			
S18	329/18	b	329	18	88	1.15	z	0.87	148.1	1.8	1.02	1.16	Q33
		p	329	108	89	1.19	y	1.00	245.4	76.4			
		v	59	90	18	1.06	x	1.02	57.7	13.5			

Table E.2. (continued)

Owens' Method Ellipsoid Calculations: Bedding Unrotated

INPUT DATA							OWENS' OUTPUT DATA						
Sample	Orientation	Plane	Strike	Dip	Rake	Ratio	Axis	Stretch	Axis Trend	Axis Plunge	Rxy	Ryz	Solution
S19	017/26	b	17	26	6	1.14	z	0.93	118.1	76.7	1.12	1.07	Q33
		p	17	116	0	1.17	y	1.00	292.6	13.3			
		v	107	90	163	1.07	x	1.12	22.9	1.2			
S20	044/19	b	44	19	143	1.15	z	0.78	98.0	54.6	1.03	1.28	Q33
		p	44	109	157	1.17	y	1.00	202.2	9.9			
		v	314	90	37	1.29	x	1.03	298.8	33.6			
S22	030/13	b	30	13	145	1.17	z	0.86	291.5	23.0	1.17	1.16	Q33
		p	30	103	170	1.18	y	1.00	47.1	45.5			
		v	300	90	105	1.26	x	1.17	183.8	35.6			
FS1	033/23	b	33	157	114	1.18	z	0.87	358.5	10.5	1.06	1.16	Q33
		p	33	67	91	1.11	y	1.00	88.6	0.4			
		v	303	90	106	1.18	x	1.06	180.8	79.5			
FS2	022/19	b	22	161	92	1.15	z	0.91	23.5	23.2	1.13	1.10	Q33
		p	22	71	130	1.18	y	1.00	284.5	20.3			
		v	112	90	72	1.21	x	1.13	157.6	58.4			
FS3	054/13	b	54	167	94	1.20	z	0.81	208.1	64.7	1.05	1.24	Q33
		p	54	77	15	1.33	y	1.00	18.6	25.0			
		v	324	90	161	1.06	x	1.05	110.3	3.7			

Plate 1. Geologic map of Barclay anticline and thrust, Pocahontas Co., West Virginia